Journal of Atmospheric and Solar–Terrestrial Physics 209 (2020) 105394

Contents lists available at ScienceDirect

Journal of Atmospheric and Solar-Terrestrial Physics

journal homepage: www.elsevier.com/locate/jastp

Research Paper

AIM CIPS PMC tracking wind product retrieval approach and first assessment

P.P. Rong [a,*], J. Yue [b,c], J.M. Russell [a], J.D. Lumpe [d], D.E. Siskind [e], C.E. Randall [f]

[a] Center for Atmospheric Sciences, Hampton University, Hampton, VA, USA
[b] Catholic University of America, DC, USA
[c] NASA Goddard Space Flight Center, Greenbelt, MD, USA
[d] Computational Physics, Inc., Boulder, CO, USA
[e] Naval Research Lab, Washington DC, USA
[f] Laboratory for Atmospheric and Space Physics, University of Colorado Boulder, USA

ARTICLE INFO

Keywords:
Cloud wind tracking
CIPS PMCs
Pattern matching algorithm
Wind assessment

ABSTRACT

The refined Cloud Imaging and Particle-Size (CIPS) cloud wind tracking algorithm is elaborated and the wind product is assessed against the Navy Operational Global Atmospheric Prediction System - Advanced Level Physics and High Altitude (NOGAPS-ALPHA) winds and the horizontal wind model (HWM14) climatological winds. Multiple searching frame sizes are adopted to generate the preliminary wind sets which are then merged and further edited based on the clustering of the similar wind directions (±20°). The mean values of the clusters within the sampling grids of 1.5 ° × 1.5 ° or 4.5 ° × 4.5 ° are taken as the final wind product. At the coincidences the CIPS and NOGAPS winds show a moderate degree of deterministic consistency. We have further shown that on the orbit-to-orbit basis when the NOGAPS modeled ice and CIPS measured ice correlate better, the wind agreement is also better. The difference in the two wind sets is most likely attributed to the NOGAPS temperature being deviated from the true temperature that will affect the geostrophic component of the winds and also to the fact that the CIPS winds are often ageostrophic and are cascaded into smaller scales. The CIPS zonal (westward) winds are decreased and then reversed in early June and late August whereas in the core of the season they are stronger. This overall variation pattern is shared by both NOGAPS and HWM14 zonal winds. Both NOGAPS and HWM14 zonal winds exhibit ~8–10 m/s difference between cases using all local times (LTs) and the CIPS LT range 13–23 h due to the dominant diurnal migrating tides, and this may partially interpret the weaker CIPS zonal winds. The meridional (equatorward) winds do not follow any established intra-seasonal variation pattern but rather the variability is susceptible to the sampling longitudes/latitudes.

1. Introduction

The tropospheric cloud features viewed in time sequence are being used to infer atmospheric motions since 1960s [Fujita et al., 1968, 1973]. Atmospheric motion vectors (AMVs) therefore are a proxy measure of wind and are indispensable to numerical weather prediction. Derived by tracking cloud or water vapor features in satellite imagery, these products mitigate critical data gaps in regions that are otherwise poorly covered by observations [Mueller et al., 2017]. The cloud motion vectors (CMVs) are derived by a three-step procedure. The initial step selects target, the second step assigns altitude, and the third step derives motion. Motion is derived by a pattern recognition algorithm that matches the feature within the targeted area in one image within the search area [Menzel, 2001]. Traditional cloud wind tracking is often carried out in the troposphere where the cloud coverage is the largest and the occurrence most frequent.

Polar mesospheric clouds (PMCs), or noctilucent clouds (NLCs) [e.g., Foerster and Jesse, 1892; Fogle and Haurwitz, 1966] are thin water ice clouds that are regularly observed poleward of 60°N/S at approximately an altitude of ~83 km which is the highest place in the Earth atmosphere water clouds could ever exist. The PMC formation is attributed to the low temperature and enhanced H_2O abundance driven by the upward transport branch of the residual meridional circulation in the polar summer region [Garcia, 1989]. The wind measurements for this altitude and latitude range are generally scarce and are mostly taken at the ground-based instrumentation networks maintained by different groups

* Corresponding author.23 E. Tyler street, Hampton, VA23668, USA.
E-mail address: ping-ping.rong@hamptonu.edu (P.P. Rong).

https://doi.org/10.1016/j.jastp.2020.105394
Received 22 April 2020; Received in revised form 7 July 2020; Accepted 14 July 2020
Available online 3 August 2020

[e.g., Portnyagin et al., 2004a; Hoffmann et al., 2011; Latteck et al., 2012; Renkwitz et al., 2018], and by a small number of satellite instruments such as the UARS High Resolution Doppler Imager (HRDI, 50–115 km, 1993–1994) and Wind Imaging Interferometer (WINDII, 90–120 km, 1991–1996) [e.g., Drob et al., 2008; 2015]. Employing PMCs or NLCs as wind tracers began as early as 1892 by Foerster and Jesse, and other successors also have carried out similar studies such as by Baumgarten et al. [2002] and Dalin et al. [2013]. Berger and von Zahn [2007] used a Lagrangian model to show that ice observed at 69°N could be nucleated 9° poleward and the averaged transport time could be as long as 36 h. Given the originality of these studies, the PMC/NLC wind tracking operation was only carried out within limited spatial region and time periods. In addition, the poor availability of the correlative wind sets would pose difficulty to the validation of the wind tracking results.

In a recent study by Mueller et al. [2017] the CMV product retrieved from the Multi-angle Imaging SpectroRadiometer (MISR) instrument on the polar-orbiting Terra satellite is assessed through coincidence analysis with several contemporary data sets of the atmospheric motion vectors (AMVs). The Terra satellite swath width is of 360 km, and the height-assigned CMVs are obtained from a single overpass by tracking feature progression within MISR red-band imagery over the 3.5-min interval between the initial 70° forward view and the nadir (0°) view and then again for the same interval between the nadir view and the final 70° aft view [Horváth and Davies 2001; Mueller et al., 2013]. Due to the small time interval and a large viewing angle difference, a 0.5 km of cloud height error (for example) can cause ~6.5 m/s of wind error along-track, which is notably large, due to the stereoscopic parallax. Also given the fact that the tropospheric cloud height varies in an extended range of 2 km–12 km, stereoscopic parallax can be a significant error source to the MISR CMVs. Features are tracked by a pattern matching algorithm applied to different resampling resolutions, i.e., 1.1 km, 0.55 km, and 0.275 km, to obtain robust matching results, with roughly consistent frame sizes of 6–8 km. Assuming a tropospheric jet speed of 32 m/s [Wu et al., 2015], after 3.5 min the cloud pattern movement is about 6.7 km which is close to the frame size and meanwhile this distance far exceeds the pixel size (i.e., 0.275 km), i.e., by ~25 times. The underlying mechanism of the MISR cloud height and motion retrievals consists of two steps, correspondence and reconstruction. That is, (1) identifying conjugates, the apparent image coordinates as captured (at different times for the same cloud feature) by two or more of MISR's nine cameras during an overpass at a given surface ellipsoid, and (2) subsequently inferring the true position (including the cloud height) and horizontal motion of each such feature by intersecting known camera lines of sight associated with conjugate image coordinates. In summary, in the first step a successful pattern matching is being achieved; and in the second step, reconstruction infers the position of the feature associated with that conjugate.

The fact that PMCs are a layered phenomenon, i.e., with a centroid height at ~83 km, enables the longitude/latitude (or lon/lat) registration more definitive than the tropospheric clouds. Russell et al. [2010] indicated that the PMC height variability could reach ~3 km throughout the season and for different hemispheres, with the southern hemispheric PMC being systematically higher. Under such an estimate the parallax still exists when the camera viewing angle is deviated from zero. In the CIPS retrieval a constant cloud deck height of 83 km is assumed [Lumpe et al., 2013] and the lons and lats are registered prior to the cloud tracking operation. The CIPS instrument is able to achieve a global coverage within a day by providing 14–15 "push-broom" orbital strips with a cross-track width of about 800 km which is about twice as wide as MISR swath. The CIPS cloud coverage achieves strong overlaps north/south of 70°N/S between orbits. This would allow all directions of wind detections so that the wind tracking results are less biased which might stem from the east-to-west orbital progress. A feasibility study on the CIPS cloud wind tracking was carried out by Rong et al. [2015] via exploring the results both on the same orbit and between two adjacent orbits using two test periods of five days in July and August 2007 respectively. In the along-track direction stacks of highly overlapped images occur and there are a total of 27 images along one orbit. The nadir and the front or aft view cameras have a viewing angle difference of maximally 60° which is similar to MISR. The spatial footprints of the four CIPS cameras, especially the forward and aft cameras, result in one bowtie shaped image assuming a constant cloud deck of 83 km as mentioned above. As the PMC height fluctuates within ~± 3 km it will cause uncertainty in the lon and lat registration. In CIPS level-2 data production images from all cameras are used to determine the lons and lats prior to the wind tracking and therefore a simultaneous retrieval of the lon/lat/height is not required. For example, the worst horizontal displacement error for a 3 km height difference is about 5 km (i.e., about one CIPS pixel size) assuming the maximum of 60° viewing angle, and the corresponding velocity difference is close to 1.0 m/s given 96 min of time interval which is small compared to the mean zonal wind speed of ~20 m/s in the PMC region.

The CIPS cloud tracking was initially applied to both the one-orbit-across and 7-scene-across (from the same orbit) cases [Rong et al., 2015]. In the 7-scene-across scenario, the time interval of the progressive images is roughly 3–4 min, which is similar to that in the MISR cloud tracking. However, the CIPS horizontal resolution varies in the range of 2–7 km which is 7–25 times coarser than MISR. Within 3–4 min a 20 m/s wind speed would lead to a merely 4–5 km of movement which is comparable to the image horizontal resolution. After the actual matching test using two 5-days periods as shown in the in Rong et al. [2015] we found that ~80–90% of the matches are only displaced by 0–2 pixels. Even a wind speed of 100 m/s, which is considered unusually large in the PMC region, only leads to 4–5 pixels of displacement in the same CIPS orbit. These displacements are too small to derive reliable wind speeds. Therefore, scenes from the same CIPS orbit are not sufficient to derive accurate winds.

The consecutive two orbits with longer time interval (i.e., 96 min) are eventually adopted for the CIPS wind tracking but the PMC patterns will likely experience considerable variation over this time mainly due to the change in the environmental temperature or H_2O. In some cases the rapid change of temperature and H_2O could simply deform the pattern to the point that it is no longer recognizable, resulting in failed match. But in many cases the pattern remains identifiable although there could be a systematic change in brightness, which may reflect the impact from the larger scale waves. This latter case will be discussed in the following section 3.4 through examining actual examples of matches.

Algorithm refining and the quality control of the derived winds are vital steps of the cloud tracking operation [e.g., Menzel, 2001], which has been extensively applied in the MISR tropospheric wind tracking described in Muller et al. [2013]. Accurately reconstructing motion vectors consisting of height and both axes of horizontal motion requires input conjugates specifying coordinates for three cameras (i.e., conjugate triplets) spanning a large viewing angle difference. A clustering algorithm is used to independently derive forward and aft 17.6 km resolution fields of modal conjugate triplets (nadir-forward-forward or nadir-aft-aft). The raw height resolved feature motion vectors reconstructed from conjugate triplets undergo flagging and quality control operations that ultimately yield the height resolved cloud motion vectors (on the regularly gridded system with 17.6 km resolution) provided to end users.

The CIPS cloud tracking was carried out between two adjacent orbits (with 96 min time difference) with no stereo vectors being retrieved because PMC height is relatively constant, i.e., 83 ± 3 km. The screening/editing strategies are designed differently but also share similarities with the MISR cloud tracking. For example, we have used different frame sizes rather than obtaining multiple conjugates from different cameras as in the MISR cloud tracking, to achieve redundancy of the wind detections. For the sake of quality control, we have sampled CIPS winds on two regularly spaced grid systems, i.e., 1.5°lon × 1.5°lat, and 4.5°lon × 4.5°lat, with shifted node positions, resulting in totally

five sets, to verify the consistency and robustness of the wind product.

In section 2 the AIM CIPS level-2 product and the Navy Operational Global Atmospheric Prediction System-Advanced Level Physics and High Altitude (NOGAPS-ALPHA) assimilated data set are described []. In section 3 the CIPS cloud wind tracking algorithm and screening/editing strategy are elaborated, and the examples of matching results are demonstrated and discussed. In section 4the wind product is demonstrated orbit-by-orbit, to compare with the NOGAPS-ALPHA winds at their coincidences. In section 5 the intra-seasonal variability of zonal and meridional winds (i.e., U and V) are compared between CIPS, NOGAPS-ALPHA, and Horizontal Wind Model (HWM14) wind sets [Drob et al., 2008, 2015]. In section 6 6 regression analysis is carried out to assess the relative importance of tides and 2–5day variability modes in the NOGAPS-ALPHA winds, and to demonstrate the potential aliasing effect of tides on the longer time scale variability in the CIPS winds. The remaining issues and conclusions are summarized in sections 7-8.

2. Data sets

2.1. CIPS level-2 PMC images

AIM satellite is a polar orbiting (i.e., 97.8° inclination angle) sun-synchronous satellite (2007-current) that was launched into a near-circular Earth orbit at ~600 km altitude above the Earth surface in April 2007 [Russell et al., 2009]. AIM crosses the equator at 12 AM/PM local times (LTs hereinafter). CIPS aboard the AIM satellite is the first PMC imaging instrument to date to obtain an extended PMC polar coverage north/south of 70°N/S continuously throughout the summer. We should however point out that the results discussed in this paper are for the northern summers only. The fact that AIM is polar orbiting and sun-synchronous will enable approximately the same LT crossing (13–23 h in the north) for a given lon as the orbit progresses westward. The CIPS instrument consists of an array of four cameras operating with a 15 nm passband centered at ultra-violet 265 nm and provides imagery of the PMCs against the background O_3 absorbed unlit atmosphere at this wavelength [McClintock et al., 2009]Different cameras can photograph the same cloud mass with a slight time lag due to strong overlaps of images in the along-orbit direction. The CIPS horizontal resolution is approximately ~2 km at the center of the bowtie and then is degraded to ~7 km toward the edges. The field-of-view (FOV) of the camera system is 80 ° × 120 °, centered right below the satellite, with the 120° axis along the orbital track. After the removal of the Rayleigh scatter which is symmetric over the scattering angle, PMC ice particle scattering phase function is obtained assuming the knowledge on the shape and distribution of the ice particles to further retrieve the PMC albedo that is defined as the would-be albedo at solar zenith angle of 90° and therefore it only depends on the total ice component of the albedo [Bailey et al., 2009].

CIPS v4.20 level-2 orbital strips are used in this study. The stacks of 27 bowties each orbit are combined to produce one orbital strip with a uniform resolution of 25 km^2. The background Rayleigh scatter removal is carried out for the entire strip assuming that the background O_3 variability does not depend on the individual pixels [Lumpe et al., 2013]. Iterations are carried out after the first guess retrieval of the ice water content until the residual Raleigh scatter approaches zero.

2.2. NOGAPS-ALPHA winds

The NOGAPS model with Advanced Level Physics and High Altitude (ALPHA) [Eckermann et al., 2004] has extended the upper boundary to about 100 km. The NOGAPS-ALPHA included the radiative heating and longwave cooling processes with the non-local thermodynamic equilibrium effect considered, the non-orographic gravity wave drags, ozone photo-chemistry processes, and the data assimilation system (DAS) component on a 6-hourly basis. The NOGAPS-ALPHA data assimilation system (NAVDAS) component consists of the Aura Microwave Limb Sounder (MLS) v2.2 temperature and H_2O in the pressure range 32–0.01 hPa [Schwartz et al., 2008], and the Sounding of the Atmosphere using Broadband Emission Radiometry (SABER) instrument on the Thermosphere Ionosphere Mesosphere Energetics and Dynamics (TIMED) satellite v1.06 temperature [Mertens et al., 2004]. Eckermann et al. [2009] used the SABER v1.07 temperature up to 0.002 hPa to correct the summer mesopause region where PMCs form, and further on corrected the v2.2 MLS temperature toward SABER so that the known MLS cold bias in the mesopause region was reduced.

The forecast component of NOGAPS-ALPHA can provide output of the 1-hourly product with the same 6-hourly forecast-assimilation cycle [e.g., Siskind et al., 2012; Stevens et al., 2017]. The 1-hourly product includes temperature, geopotential height, and winds but does not include H_2O. Unlike the 6-hourly product which is on a 360 × 181 × 60 (1° horizontal resolution) grid system, the 1-hourly product is on the 240 × 120 × 74 (1.5° horizontal resolution) with the upper boundary extended from the originally 0.0005 hPa to 0.0001 hPa to cover lower thermosphere. The 1-hourly product is used in this study because the time coincidences can be achieved more closely and also it has a pressure grid of 0.00436 hPa which matches the PMC height more precisely than the 0.0036 hPa in the 6-hourly product.

The NOGAPS-ALPHA assimilation does not include any middle atmospheric wind measurements. Rather, the NAVDAS calculates correlated temperature and wind increments based on a gradient wind approximation. The assimilated wind and temperature fields are further constrained by the physical parameterizations of the atmospheric model (e.g., gravity wave drag, diffusion) [McCormack et al., 2009]. The NOGAPS-ALPHA and the Metero radar wind measurements reach close agreement at 54°N and 88 km of altitude throughout July and August 2007, which was considered beyond expectation considering the fact that no wind information is assimilated into the NOGAPS-ALPHA [McCormack et al., 2014]. Via wave analysis, Eckermann et al. [2009] found spectral peaks of westward traveling quasi-5day and 2day wavenumbers 1–2 and a strong migrating diurnal tidal component at 65°N and 0.006 hPa in both temperature and winds. McCormack et al. 2014 showed that the quasi-2day wavenumbers 3–4 are the dominant spectral peak at 40°N/S and 0.01 hPa, and furthermore it shows that the high amplitude zone of this component extends toward higher latitude and altitude with a broad maximum occurred at 40°-70°N/S and 0.001 hPa. Both studies indicate widespread tidal variability and 2–10day/-wavenumbers 1–4 planetary scale variability in winds, temperature, and H_2O.

3. Algorithm

3.1. Rationale of the matching frame-size

Matching frames to enclose the cloud features are required to carry out the pattern matching. Before choosing the matching frame size, we resample the CIPS level-2 “push-broom” orbital images on a roughly 5 km × 5 km universal gridding system in both lon (i.e., Δlon enforced by 5 km) and lat (i.e., Δlat = 0.05) directions, shown in Fig. 1a. The purpose of the resampling is to precisely define the matching frame and to register the preliminary wind products on a universal spatial gridding system. A frame-size of approximately 500 km × 400 km (lon × lat) is taken as the default, which is the same as used in Rong et al. [2015]. The 500 km refers to the length in the lon direction at the low-lat limit of the frame, and it is reduced to 458 km at the central line of the frame. The maximum speed required for a movement over a full frame size within 96 min is approximately 80 m/s or 70 m/s in lon or lat directions, which is close to the maximum wind speeds in this altitude range. Stober et al. [2012] indicates that using a running window of ~1 h centered at the mesopause (~80–95 km) in July, the zonal winds measured by the Middle Atmosphere Alomar Radar System (MAARSY) on the island of Andøya (69.11°N, 15.76°E) fluctuates in the range of −100 m/s to 70 m/s whereas for the meridional winds the lower limit is slightly lower,

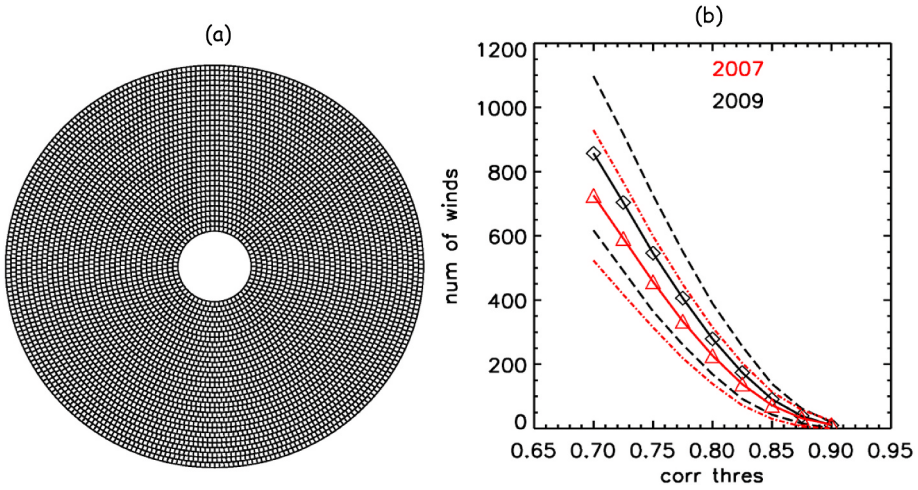

Fig. 1. (a) The grid system used for the CIPS wind tracking pattern matching. The grid length is 5 km in both lon and lat directions but here for demonstration purpose we have shown as 50 km grid length. (b) Daily mean number of wind detections based on different correlation coefficient thresholds. The dashed lines are standard deviation for July mean detection number over different correlation coefficient thresholds (solid lines).

reaching only −70 m/s [Renkwitz et al., 2018; Lübken et al., 2004].

For a given cloud feature enclosed within a frame in the current orbit, the optimum match from the next orbit is searched within one (default) frame-size of domain in all directions by an increment of 5 km. To obtain multiple winds within the current orbit, the frame is moved around by a step of every 1/3 frame-size to capture different cloud features. The 1/3 frame-size is a sufficiently small step because the wind product resolution will be no better than the frame-size itself. Smaller steps produce more redundant wind detections so that the wind field will be less fluctuating. The choice of the 1/3 frame-size is to balance between the computational efficiency and a sufficiently dense spatial coverage of the wind detections. In general a larger group of pixels represent less random cloud features and therefore will maintain better consistency between the two adjacent CIPS orbits. Better consistency between the progressive patterns points to a higher probability of successful match. On the contrary, a smaller area of clouds is less likely to be recognized after 96 min. The physical rationale of this argument is associated with the PMC lifetime that is not yet fully characterized or quantified so far. A smaller cloud pattern however is more likely to achieve a higher correlation with an irrelevant cloud pattern that is further away from one frame size.

The best match of a cloud pattern is defined by the highest Pearson correlation reached, in the next orbit within ± default frame size in both lon and lat directions. If the highest correlation of the two patterns does not exceed 0.7, then it is considered a zero match. The 0.7 threshold is empirically chosen to ensure a sufficiently large number of detections per day. Fig. 1b shows that the wind detection number exceeds 1000 per day with a standard deviation (STD) of about 200, but this number rapidly decreases as the threshold correlation coefficient increases. For example, when a 0.8 threshold is used the number of detections rapidly decreases to ~30%. But what is worth pointing out is that the wind detections using the 0.8 threshold are not proven to be significantly more reliable, which requires a separate investigation in the future.

3.2. A hierarchy of frame sizes

In the CIPS cloud wind tracking where pattern matching has a relatively low success rate due to the longer time interval, the reliability of the wind detection critically depends on two factors: one is the distance of the horizontal movement, and the other is the correlation coefficient reached. Both a smaller displacement and higher correlation coefficient will lead to more reliable detections. The high correlation ensures that they are the same cloud mass, while the smaller displacement reduces the possibility that these cloud masses resemble each other by chance. It is nevertheless not possible to entirely rule out false matches. Another factor that may impair the validity of the CIPS wind tracking is the possibility that traveling waves produce false matches due to the repeated troughs and ridges. Such cases are rare because most cloud patterns exhibit uniquely identifiable mostly irregular shapes so that the impact from waves, especially of the planetary scales, will likely be reflected by systematic changes in brightness between the 96 min, which will be discussed in section 3.4 4.

A hierarchy of three frame sizes, 0.75 × default size, default, and 1.25 × default size, are adopted to carry out three sets of pattern matching calculations. The main purpose of adopting three frame sizes is to construct a redundant and eventually merged set of winds. Twenty-five percent of the frame size change does not alter the fact that they all belong to a size range that far exceeds the pixel size and that encloses a cloud pattern that most likely will remain recognizable after the 96 min given some degree of variation. In the previous PMC model studies the PMC lifespan can reach up to 24–48 h [e.g., Jensen and Thomas, 1988; Rapp et al., 2002], which is many times longer than the 96 min and will support the validity of cloud tracking. While in practice PMCs appear to change more rapidly due to temperature and H_2O variability. Nevertheless, Rong et al. [2015] showed that between adjacent CIPS orbits the PMCs with brightness change by 50% within the same frame location, either halved or doubled, take up only ~15% of the cloud population. This will indirectly support a significant degree of stability in the PMC patterns between the 96 min.

To further explore the PMC pattern stability, or “memory”, over the 96 min, we next characterize each frame size with a histogram of the correlation coefficients at the same frame locations and then register each coefficient with a wind speed assuming wind advection is the sole mechanism of variability, which is shown in Fig. 2. The correlation coefficient would have a one-to-one correspondence to the displacement of a cloud pattern if the dominant spatial scale is wavenumber-1 in a sinusoidal form and the wind advection is the sole mechanism to drive the cloud pattern variation. The dominance of the larger scale variability within a 400–500 km frame is proven to be the case in the CIPS clouds in Rong et al. [2018]. The bottom x-axis is the correlation coefficient which varies from +1 to −1, corresponding to the sinusoidal phase shift from zero to 180°. The wind speed corresponding to the correlation coefficient of −1 provides a more stringent upper limit for the winds because it corresponds to a half frame-size movement. The wind speeds registered at the top x-axis are the mean values within each bin with non-zero correlation coefficients from the actual CIPS analysis. Three arbitrarily

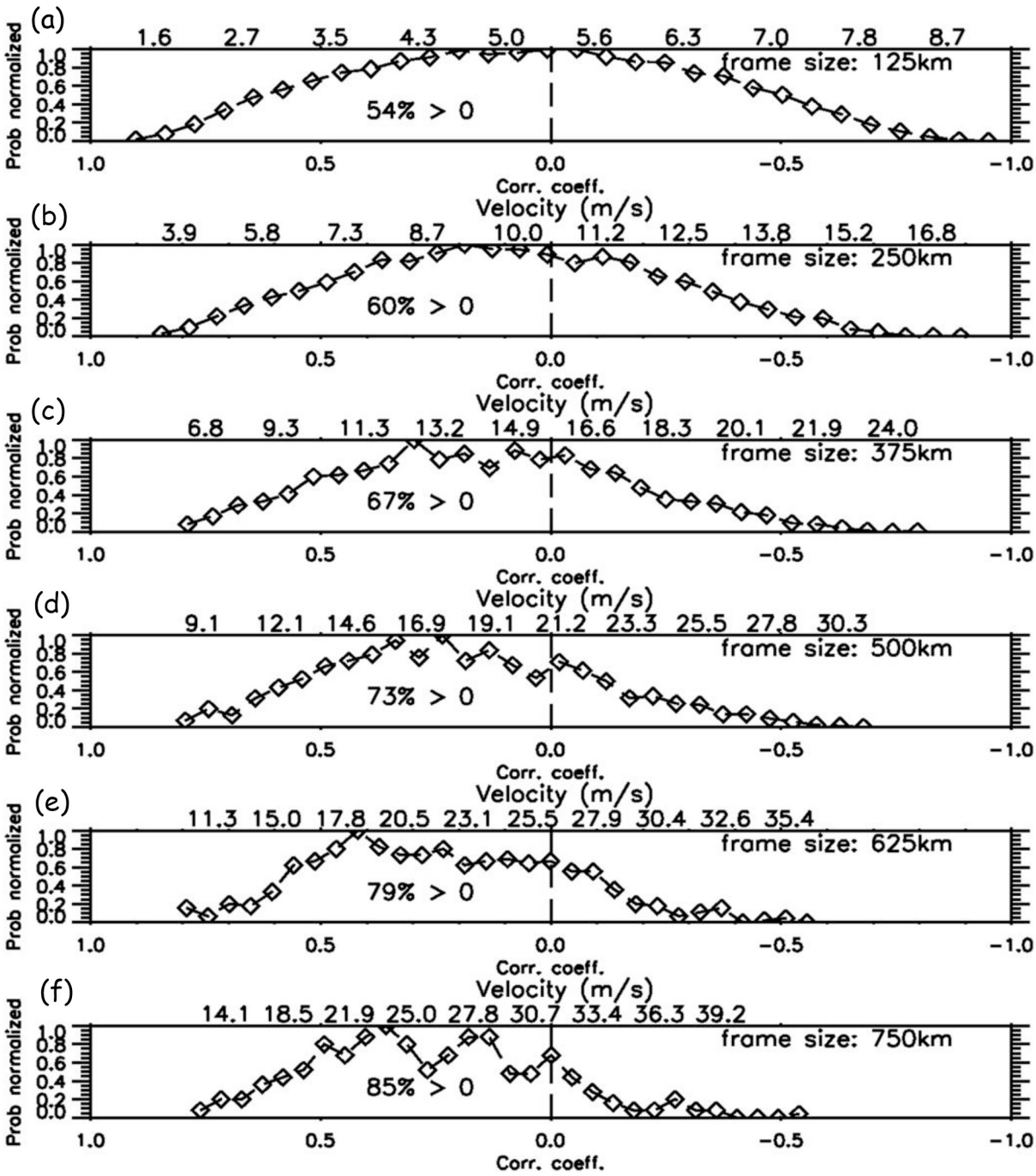

Fig. 2. The histograms of the correlation coefficients of the same-location cloud features between two orbits (i.e., 96 min apart) within the given frame. The different panels are different frame sizes. The DOYs 191, 193, and 195 in 2007 are used to build these statistical sets. The wind registration on the upper horizontal axis is based on the assumption that a wave-1 sinusoidal cloud pattern is displaced by wind advection solely.

selected days in the summer of 2007 are used to explore this statistics.

Fig. 2a indicates that for the frame-size of 125 km, about 54% of cloud population appears to possess a memory of the original pattern via showing a positive correlation. Statistically it points to a mildly positive but virtually zero memory, and therefore the wind speed at the top x-axis is not much indicative. Some of the positive correlation coefficients could have been achieved randomly because cloud features enclosed in smaller frames are prone to higher correlation. The 125 km is therefore not an appropriate frame-size to use in the CIPS wind tracking. The memory is increasingly improved as the frame size increases. For example, for the frame size of 625 km, 79% of the cloud population has a positive correlation with the original pattern. The largest wind speed registered at non-zero bins of the histograms are about 25 m/s, 30 m/s, and 35 m/s for the frame sizes of 375 km, 500 km, and 625 km respectively. The wind speed thresholds yielded for the three frame sizes are in terms of the full velocity speed $\sqrt{U^2+V^2}$ where U and V are zonal and meridional velocities. These thresholds are adopted to generate a subset of winds, or so called "more reliable" winds, to inspect the cloud tracking results from a different perspective. But we should point out that CIPS cloud wind tracking, even without these newly registered thresholds, may succumb to a bias toward weaker zonal winds because the result is not reliable for longer distance displacement.

This analysis implied that we should choose larger frames since they possess better memory after 96 min, but a larger frame will technically

reduce the number of wind detections because we will have fewer independent cloud features. In addition, an indefinitely larger frame will embrace more complex cloud features that are driven by inhomogeneous cloud physics or dynamics, which will reduce the success rate of the pattern matching and also eventually reduce the number of the wind detections. This later point however cannot be verified because we are unable to examine sizes much greater than 750 km due to the fact that the cross-orbit width of the CIPS orbital strip is ~800 km [Lumpe et al., 2013].

3.3. Screening/editing strategies

In order to apply the screening/editing procedure we first merge the preliminary wind products from using the three frame sizes. Upon merging the preliminary wind products the minimum horizontal spacing is reduced to roughly 1/3rd of the frame size 375 km. The merged winds will be eventually resampled on the NOGAPS-ALPHA 1-hourly product grid system (1.5 ° × 1.5 °) and a grid system three times coarser. The 1.5° lon and lat bin-size north of 70°N (i.e., 57 km × 167 km at this latitude) is adopted to conveniently compare with the NOGAPS-ALPHA winds. On average, the preliminary CIPS wind product spacing is roughly 153 km × 133 km based on the default frame size, where "153 km" is the length in the lon direction along the central line of the frame. This spacing is comparable to the spatial resolution of the NOGAPS-ALPHA winds. The coarser grid system of 4.5 ° × 4.5 ° is used because it is close to the actual spatial resolution of the wind product.

After choosing the sampling grid-size, different nodes are used. In the 1.5 ° × 1.5 ° (lon × lat) case we use two types of nodes, one is the original NOGAPS-ALPHA 1-hourly grid system, and the other is the NOGAPS-ALPHA grid with a half grid-size shift. In the 4.5 ° × 4.5 ° (lon × lat) case three nodes are used, zero-shifted, 1.5° shifted, and 3° shifted, respectively. Different sampling grids along with different nodes are used to rule out any possible uncertainty induced by a specific sampling process.

The screening/editing strategy is required within each sampling grid because winds can be contradictory due to the false matches caused by the inherent limitation of the wind tracking approach. Within the sampling grid we first divide the winds into clusters with each cluster possessing two or more wind values and the directional difference for each pair of these winds being smaller than 20°. Any individual wind that does not pair up with any other wind in the sampling grid-cell is removed. On the contrary, if any individual wind is involved in many different pairs then its direction will be closer to being representative to the mean wind direction within the given sampling grid-cell. The clusters of winds are then averaged to create the mean wind of the sampling grid-cell. If there is no pair at all, the wind with the minimum speed will

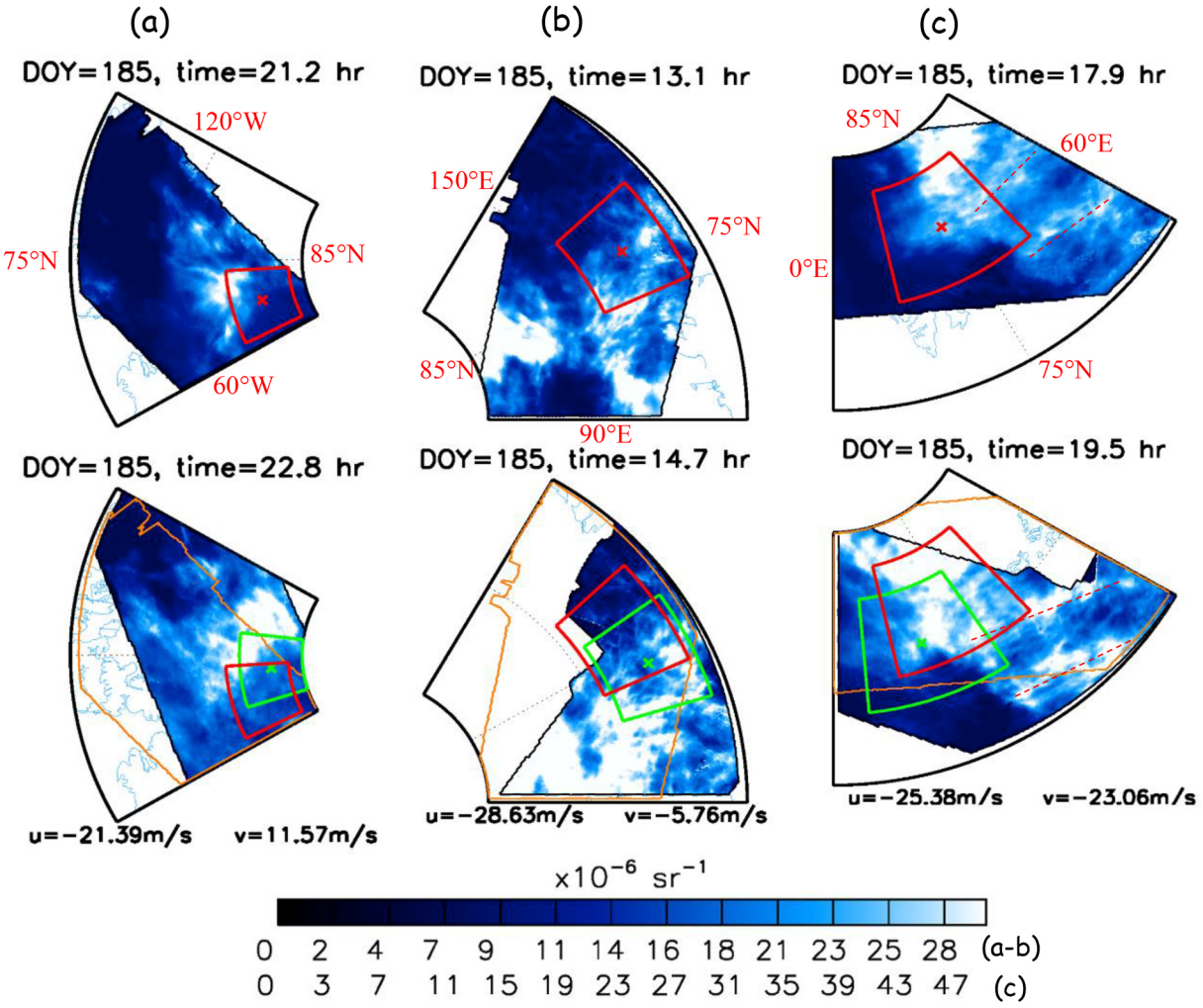

Fig. 3. Demonstration of the three frame sizes (a–c) for the pattern matching wind determination. The upper and lower panels are two consecutive orbits that are 96 min apart. Red is for original frame position and green encloses the cloud pattern that is the best match from the next orbit. The orange color in the lower panels marks the position of the first orbit. In (c) the thin dotted red lines indicate possible straight wave ridges in this particular case. The same polar projection is applied to all maps with the vertical line below the north-pole (not shown) being at the 0° lon, and the lon and lat limits are marked for each map). In (a–b) the color-bar maximum is 30 × 10^{-6}sr^{-1} while in (c) maximum is raised to 50 × 10^{-6}sr^{-1}.

be selected as the value of the sampling grid-cell since a small displacement is considered more reliable in the CIPS cloud tracking. In many cases this approach will virtually exclude any singular winds that are drastically different from the rest of the winds within a given sampling grid-cell. But to implement the approach to its fullest extent we must have highly redundant winds within a given sampling grid-cell which is not yet the case unless wind tracking is carried out by a step much smaller than 1/3rd of frame-sizes.

3.4. Elaboration of three pattern matching examples

In order to gain a tangible understanding of the CIPS cloud pattern match, Fig. 3 shows examples of using the three frame sizes respectively. The selected matches are characterized by speed values ($\sqrt{(U^2+V^2)}$) that are very close to 25 m/s, 30 m/s, and 35 m/s which are the wind thresholds in the constrained cases. Fig. 4 that follows shows the corresponding images that are exactly enclosed in the frames so that we are able to further examine the similarity of the cloud structures between the two CIPS orbits.

In all three panels of Fig. 3 we discovered some degree of sudden increase of overall brightness between two orbits both inside and outside the matching frames, which may have stemmed from the larger scale wave effect, i.e., 2–5day planetary waves or tides, in temperature or H_2O. For example, a 2day wave would travel about ~345 km within 96 min at 75°N, which is a sufficiently long distance to cause systematic temperature change within the frame. It is also worth pointing out that such a sudden change of cloud brightness between adjacent orbits is a regular occurrence in CIPS and may be worth a separate investigation. The brightness change however does not directly affect the pattern matching result because it is the recognizable irregular pattern shape that serves as the identity of a cloud mass; in Fig. 3a the pattern is drifted north-west and in Fig. 3b it is mostly toward the west. It is worth mentioning that Fujita et al., [1973] also showed an example of cumulus cells growing larger and dissipating during a cloud tracking process. In Fig. 3c there are signs of straight wave structures outside of the matching frames indicated by the red dashed lines and the orientation of the waves appear to have slightly changed between two orbits. It is unclear how much gravity wave propagation could have contributed to the variability on the later orbit. It could have been that the entire cloud mass turned brighter and meanwhile was drifted south-west. This could very likely be the case based on the prediction by Fogle and Haurwitz [1966]. Another noteworthy feature, which has occurred more than occasionally in the CIPS PMCs, is that the semi-organized small scale (e.g., wavelength of ~20–60 km) wave structures within the frame suddenly become either more or less distinct on a later orbit (after 96 min) without any clear indication of propagation. Revisiting the detailed small scale gravity wave structures in Fig. 4b we find that the "lattice" shaped interfering wave structures are present on both orbits but in the later time frame they appear more distinct. We will in the future examine how these pairs of wave structures differ in a statistical sense in the CIPS cloud tracking frames and what mechanism controls their evolvement.

4. Coincidence analysis with the NOGAPS-ALPHA winds

We next will use the NOGAPS-ALPHA 1-hourly winds, NOGAPS hereinafter, on the pressure surface of 0.00436 hPa (~84 km) to compare with the CIPS cloud tracking winds. NOGAPS is adopted as the first data set to assess the CIPS wind tracking product because it is available on a regular gridded system (1.5°lon × 1.5°lat) with the full 3-D coverage throughout the 2009 summer so that coincidences exist for all individual CIPS winds. It has been used in several previous PMC studies such as in Stevens et al. [2010; 2017] but their main focus was not on the very high latitude region (i.e., 70°-86°N). The following analysis is a mutual assessment process to examine the consistency between CIPS and NOGAPS in a broad spectrum. NOGAPS is a combination of the model prediction and DAS system. The model included the radiative heating and cooling and the gravity wave drag to be able to resolve tides and other planetary scale variability along with the meridional circulation.

4.1. CIPS ice versus the 0-D modeled ice

Prior to the wind comparison we first examine whether the NOGAPS zero-dimensional (0-D) modeled ice [Hervig et al., 2009] and the CIPS ice reasonably agree in a statistical sense, which serves to examine the more fundamental consistency between CIPS and NOGAPS. We have learned that in NAVDAS temperature and wind increments are linked to each other via gradient wind approximation. Temperature also plays a strong role in the 0-D model in which super-saturation immediately results in the ice production and the full amount of H_2O in excess of the frost point is turned into ice.

For each orbit per day we have used the NOGAPS temperature and H_2O at the coincident lons/lats/universal time (UT) (with CIPS) to carry out the 0-D calculations throughout the whole season. We should point out here that a roughly 5 K correction toward warmer state is applied to the NOGAPS temperature to alleviate the known cold bias [Stevens et al., 2017]. Over each orbit a spatial correlation coefficient between the CIPS measured ice and the NOGAPS 0-D ice is calculated.

The histogram of the coefficients (shown in Fig. 5a) indicates that the positive correlation dominates but there is a significant fraction of negative coefficients which point to poorly correlated 0-D ice and CIPS ice in these particular cases. A closer examination to specific pairs (not shown here) indicates that in many cases with weak positive

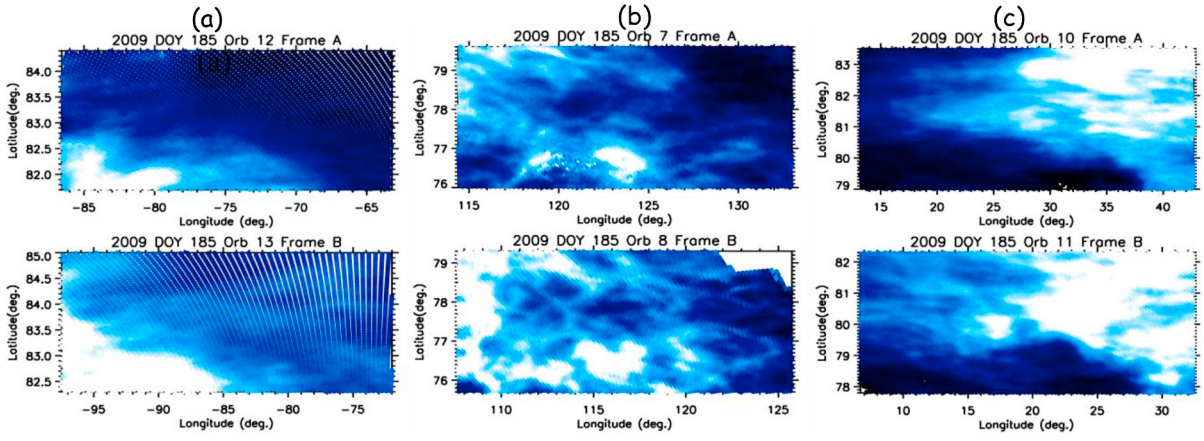

Fig. 4. The cloud features enclosed in the red (upper) and green (lower) frames in Fig. 3 respectively.

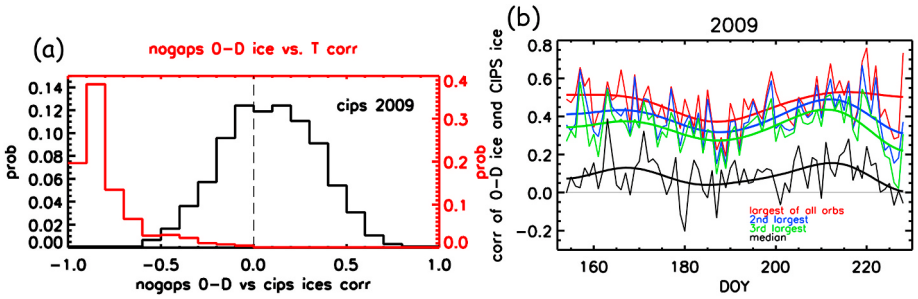

Fig. 5. (a) Black: histogram of correlation coefficients (over any given CIPS orbit) between the NOGAPS 0-D ice and CIPS measured ice at the coincidences throughout the summer in 2009. Red: same as the black except for correlation coefficients between the NOGAPS 0-D ice and the temperature used to generate the 0-D ice. (b) Intra-seasonal variations of the daily largest to median correlation coefficients between NOGAPS 0-D ice and CIPS measured ice.

correlations, larger scale zonal variabilities of the NOGAPS 0-D ice and the CIPS ice roughly agree but this does not ensure high positive correlation since the CIPS ice exhibits stronger cascading toward smaller scale features compared to the 0-D ice. In some cases especially, the variability patterns agree over only a fraction of the zonal circle. The red colored histogram in Fig. 5a indicates that the 0-D ice holds a strong anti-correlation with (the NOGAPS) temperature and therefore temperature almost entirely controls the 0-D ice variability.

Fig. 5b shows the daily time series of the correlation coefficients between the CIPS measured and 0-D modeled ice, confirming the overall weak but definitely positive correlation and furthermore the leading three largest coefficients are distinctly higher. The fact that the NOGAPS temperature deviates from the true temperature of the atmosphere could be one of the main causes for the discrepancy between the 0-D ice and CIPS ice, probably due to the NOGAPS model physical constraint and the accommodation between the MLS and SABER measured temperature in the DAS component that is incorporated on a 6-hourly basis.

4.2. Demonstrate the wind agreements at the coincidences

The CIPS wind detections are overlapped on the CIPS PMC albedo map on the orbit close to the UT hour 21, on DOY 185 of 2009, to demonstrate the sanity of the cloud tracking result, shown in Fig. 6. We should point out that in this display the zonal and meridional winds used the same scale but due to the ratio of the display the meridional winds appear dominant. In practice the zonal winds should be about 5-times stronger than what is observed here, as shown in the legend. The CIPS winds determined using these two orbits are toward north-west and south-west directions respectively split at lon of 30°W, indicating reversed meridional wind directions between the two lon sections. The albedo distribution roughly echoes such a directional move of clouds although the cloud brightness is notably strengthened in the later orbit. The brightness change was argued to be caused by tides or planetary waves.

The wind agreement and discrepancy at the CIPS and NOGAPS coincidences for the same orbit are shown by different colors in Fig. 7. The agreement here refers to both the zonal and meridional winds having consistent directions between the two wind sets. In the lon section 100°W - 30°W, both CIPS and NOGAPS echoed a westward and poleward flow. In the lon section of 30°W - 10°E the agreement with NOGAPS is much poorer (see Figs. 7a and 7b). In Fig. 7c the full NOGAPS wind vector field at the same UT hour is overlapped on the geopotential

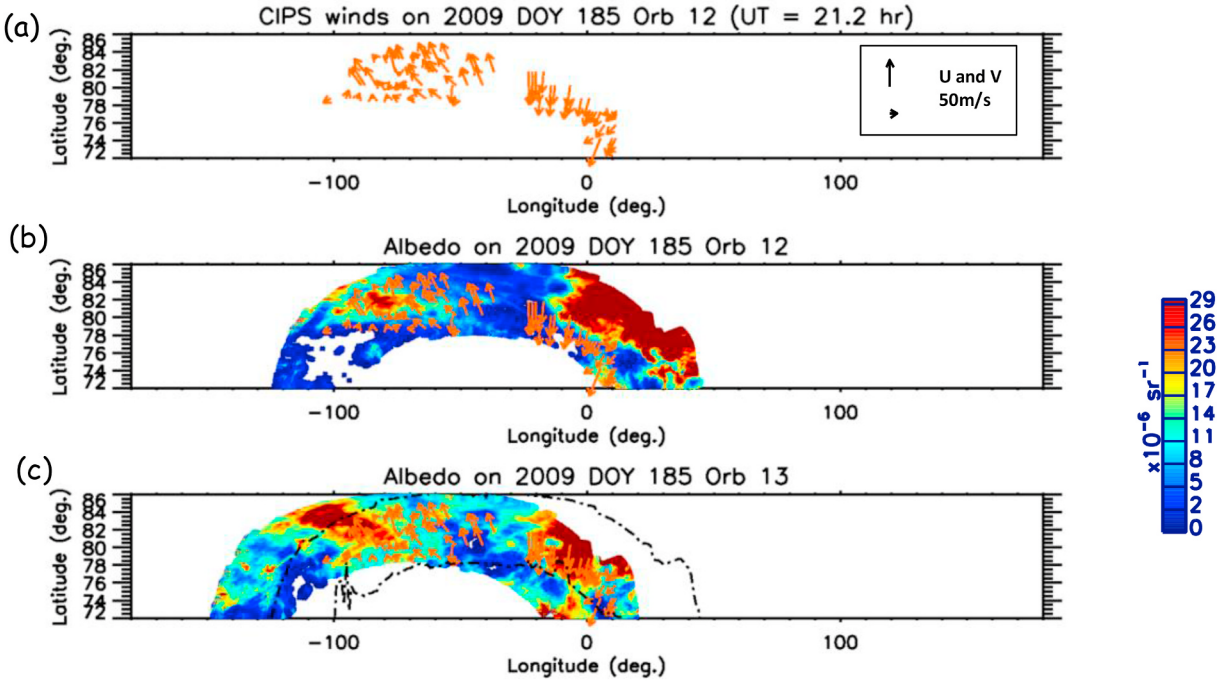

Fig. 6. The demonstration of the CIPS cloud tracking winds overlapped on the CIPS albedo orbital strips. The orange vectors are identical for the three panels while in (b) and (c) the color-filled fields are CIPS albedo over the two adjacent orbits. The legends of zonal and meridional winds (U and V) of 50 m/s exhibit different lengths due to the display ratio.

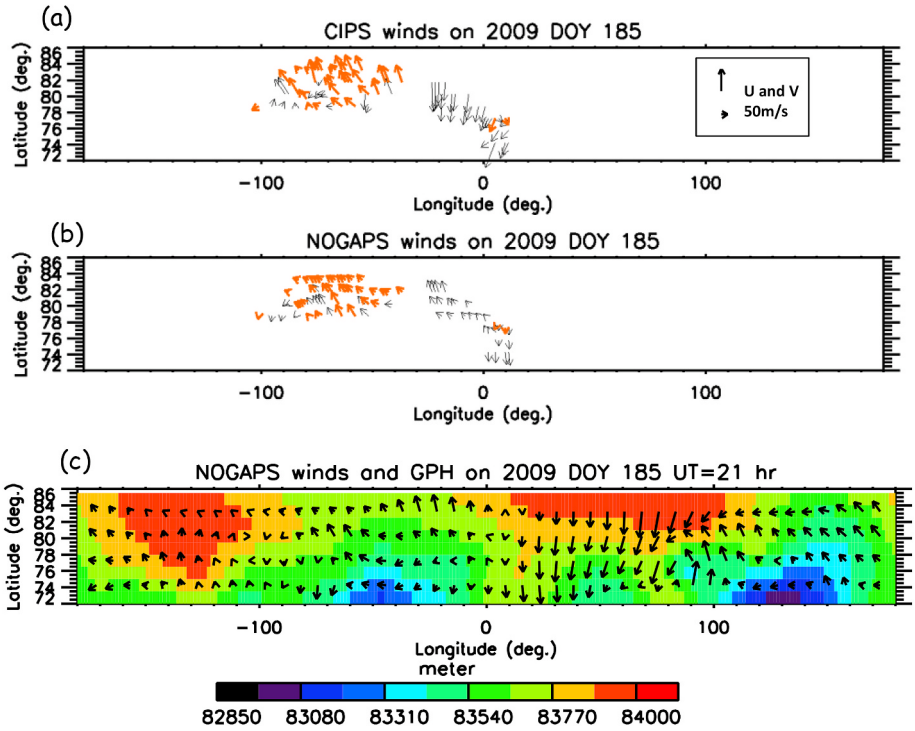

Fig. 7. (a–b) The CIPS and NOGAPS winds with consistent (thick orange) and inconsistent (thin black) directions in both zonal (U) and meridional winds (V) at coincidences on DOY 185 2009 on the CIPS orbit close to UT hour 21. (c) NOGAPS winds (black arrows) and geopotential height field (color-filled) on the NOGAPS grid points in the same latitude range (72°-86°N).

height field, which demonstrates that the left side of the winds is characterized by lower geopotential height in a majority of cases since gradient wind approximation is used in the NOGAPS-ALPHA. From Fig. 7c we can see that the reversal of the meridional winds did also occur in the NOGAPS winds but in a further down lon section of 0–100°E due to the less rapid variability along the zonal circle. Such a phase difference is noted often in both ice and winds between CIPS and NOGAPS. Several factors may contribute to the potential discrepancies; first, the NOGAPS temperature deviates from the true temperature which would affect its wind product; second, the CIPS winds captured a larger abundance of smaller scale variabilities which are ageostrophic in nature likely reflecting the mean flow variation due to gravity wave breaking [e.g., Fritts et al., 2015]. It is also noteworthy that in both CIPS and NOGAPS results the wind directions are roughly consistent over a large part of 70°–86°N, pointing to a relative weak latitudinal dependence of the winds.

The wind agreements at the coincidences throughout all orbits (or UT times) for the same DOY 185 2009 (Fig. 8) suggest that they are widespread but are unbalanced in numbers between different orbits. The

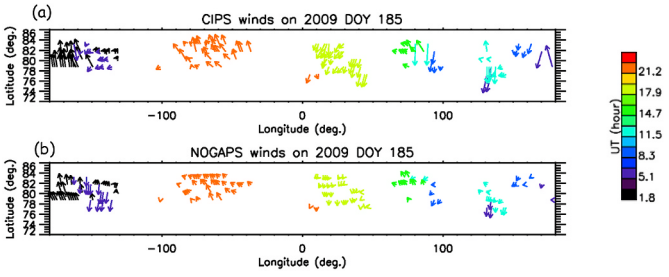

Fig. 8. Demonstration of CIPS (a) and NOGAPS (b) directional agreements (in both U and V) on all the orbits for DOY 185 2009, with the rainbow colors (black to red) representing smaller to larger UT hours. Wind vector legend is the same as in Figs. 6 and 7.

generally consistent westward directions over the different orbits point to the existence of the migrating tides in the zonal winds or a genuine zonal mean easterly, while the frequent reversals of the meridional wind directions suggest that either higher frequency of tides or non-migrating tides may have contributed significantly.

4.3. Statistics of the full season

We next examine the statistics of the agreements throughout all the summer DOYs in 2009. Fig. 9 shows the scatter plots of total number of the CIPS winds per day versus number of agreements with NOGAPS, with and without wind speed thresholds applied. For each day all wind detections are included regardless of the orbits/UT times. It shows that if we focus on the zonal or meridional winds only, the fraction of agreement exceeds 50% by 1–6% at the coincidences. When both zonal and meridional winds are required to be consistent between CIPS and NOGAPS, the fraction of agreement exceeds 25% by 4–6%. Both percentages indicate that averaging over all orbits there is still a modest degree of deterministic consistency between the CIPS and NOGAPS winds. It is also worth mentioning that the "reliable" winds with thresholds applied show qualitatively the same but slightly better result which is not sufficient to conclude that more accurate cloud wind tracking will improve the degree of agreement.

The CIPS winds and NOGAPS winds do not show the same degree (i.e., 29–31%) of agreement on all orbits/UT times. Rather, the percentage is highly unbalanced between orbits. The same asymmetry between orbits is also shown in the ice comparison in Fig. 5b. We suspect that on some orbits CIPS and NOGAPS may maintain better consistency in both ice distribution and wind directions. Figs. 10a-b shows the intra-seasonal variability of the leading three higher agreement numbers (per orbit) divided by the median agreement numbers (per orbit). The spikes of the ratio reaches 10 which suggests that the numbers of the CIPS and NOGAPS wind direction agreements are much higher on the three out of the 14 orbits. In Fig. 10b when the agreement criterion tightens to a 10° of directional difference the result is qualitatively the

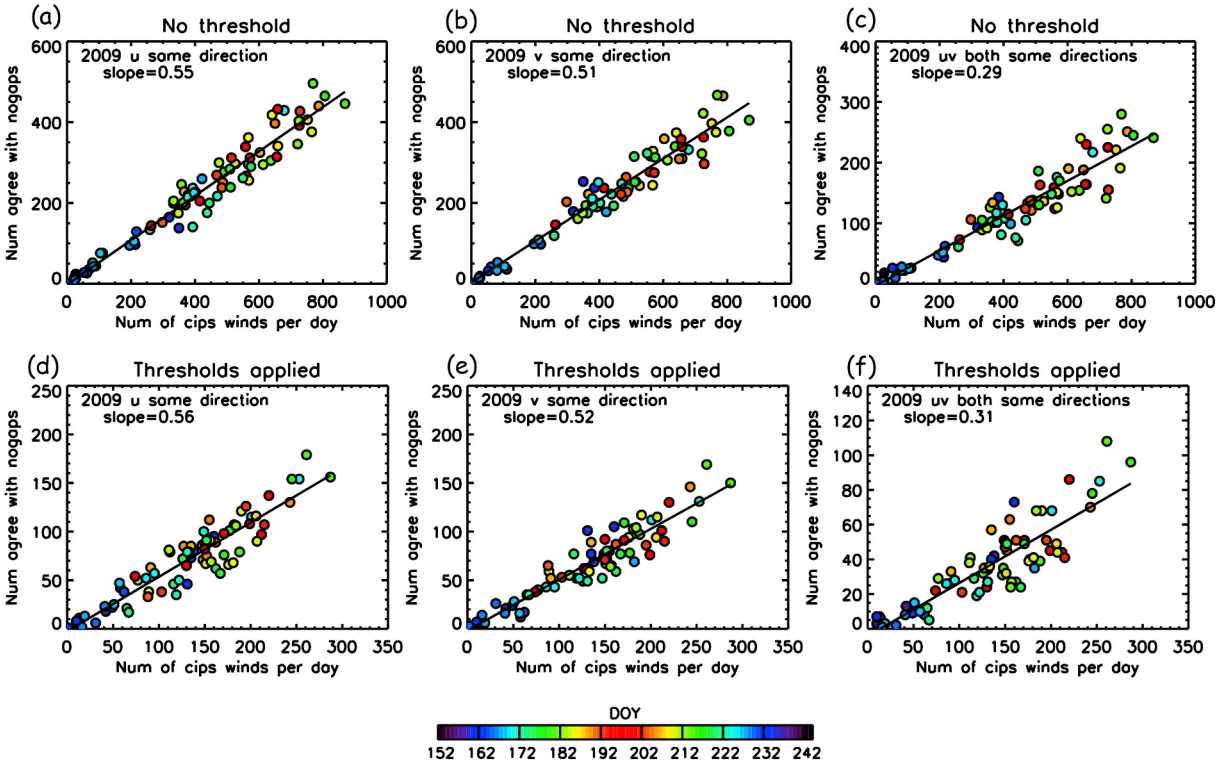

Fig. 9. The fraction of agreements, i.e., characterized by the slope in the legend, between the CIPS and NOGAPS winds at the coincidences over the entire season. The (a) and (d) are for U agreements only, (b) and (e) are for V agreements only, and (c) and (f) are for cases of both U and V being in consistent directions between the two wind sets. Upper and lower panels are for cases with and without wind thresholds respectively. The wind thresholds are elaborated in Fig. 2.

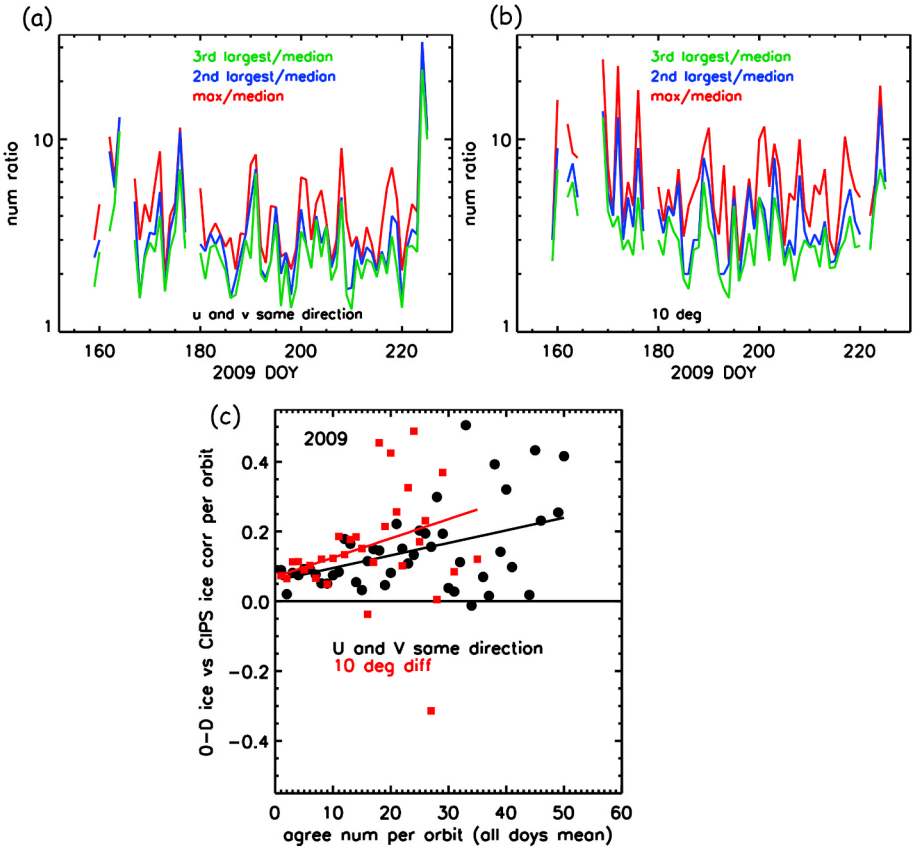

Fig. 10. (a)–(b) The daily time series of the ratios between the largest, 2nd largest, or 3rd largest agreement numbers and the median wind agreement number per orbit. This indicates that wind agreement numbers between CIPS and NOGAPS are highly unbalanced among the CIPS orbits. The (a) and (b) used different criteria to determine directional agreement between the two wind sets as indicated in the legend. (c) The relationship between the ice agreement and wind agreement per orbit. The ice agreement is characterized by the spatial correlation coefficient of the modeled and measured ice, and the wind agreement refers to the directional agreement as defined above.

same except that the asymmetry between orbits becomes stronger, further confirming the unbalanced numbers of wind agreements between orbits.

To further quantify the relationship between the ice distribution consistency and the wind direction agreement, we pair up the ice correlation coefficient and wind agreement number for each orbit on a daily basis and do find a positive slope even though a fairly large scatter exists, shown in Fig. 10c. The slope is larger for the stricter 10° criterion case indicating a more distinct relationship between the ice distribution consistency and wind agreement number. Such a relationship exists probably because both the NOGAPS 0-D ice and winds are associated with temperature. The large scatter suggests that other factors are in play such as the inherent limitation of cloud tracking approach and the ageostrophic nature of the CIPS winds.

5. Intra-seasonal variability of the winds

The global general circulation in the mesosphere is transitioned into distinctly different regimes between different seasons, reflected by the clockwise to anti-clockwise reversal of the residual circulation between hemispheres from summer to winter [e.g., Garcia and Solomon, 1985]. As a result, we would expect weakened westward or equatorward winds at the start and end of summer. Due to the generally poor spatial and temporal data coverage of wind measurements, to this date the detailed intra-seasonal variability in the polar region for individual years has rarely been discussed. The monthly climatology at the PMC height indicates that zonal (westward) winds accelerate throughout April, May and June, reach the maximum prior to mid-July, and then decelerate in August and further are rapidly reversed to eastward winds in September [Portnyagin et al., 2004b; Dowdy et al., 2007; Lukianova et al., 2018].

The spatial and temporal sampling condition of the CIPS winds is the first aspect to understand in order to further examine any daily mean behavior of these winds since it may greatly affect the magnitude and variability of the winds. The CIPS LT coverage in three representative days, DOYs 152, 183, 214 of 2009, are shown in Fig. 11a which indicates a consistent and continuous coverage in the range of 13–23 LT hours, suggesting that CIPS only covers the 2nd half of the day in the northern polar summer. If tidal variability is strong (see section 6) partial LT coverage may serve as a key factor to constrain the overall magnitude of the CIPS zonal winds. Fig. 11b shows that in both 2009 and 2007 the daily mean latitudes of the CIPS winds remain fairly constant by staying at 81°N or slightly higher but toward the start and end of the season the fluctuation becomes stronger suggesting more uncertainty stemming from smaller number of wind detections. There is a fairly broad standard deviation (STD) of 1.9° reflecting the fact that the wind detections are widespread north of 75°N. The slight differences between the years 2009 and 2007 do not substantially affect the intra-seasonal variability of the winds because the latitudinal gradient of hourly NOGAPS horizontal wind field is generally small and moreover such a gradient is not consistent throughout the day (not shown here), which would prevent a systematic impact on the daily mean values.

The daily mean time series of the CIPS zonal winds in the 2009 and 2007 polar summers and the NOGAPS winds on the coincidences (with the CIPS winds) are shown respectively in Fig. 12. The NOGAPS winds are sampled at both years' coincidences to explore whether the intra-seasonal variability is susceptible to the small changes in the sampling lons and lats. Universally in all cases in Fig. 12 the westward winds prevail with widespread transient day-to-day fluctuation. The 2nd-order polynomial fitting curves exhibit distinct acceleration and deceleration of the westward winds in early June and late August in both years in the CIPS winds although short excursions of larger winds can occur at both the start (i.e., in 2007) and end (i.e., 2009) of the season creating asymmetry in the polynomial fit. The approximate timing when seasonal maximum zonal wind is reached is in early to middle July which approximately agrees with what Lukianova et al. [2018] has shown over the years 2009–2015. Generally speaking the timing when maximum zonal wind is reached could be dependent on year or lon/lat [also see Dowdy et al., 2007]. The daily mean CIPS zonal wind reaches seasonal maximum of ~15–20 m/s with the standard error of the mean (SEM) staying within ~1.5 m/s on average suggesting an uncertainty that is far below the actual magnitude in most cases. However toward the start and end of the season, due to the smaller numbers of wind detections, the SEM could reach 7–10 m/s (not shown here) suggesting poorer reliability of the daily mean winds during these times.

The more "reliable" CIPS wind subset with smaller speeds comprises about 30% of the CIPS wind detections, and the polynomial fit indicates an almost constant level of zonal winds throughout the season with no distinct intra-seasonal variability except that in August 2007 the decrease of the westward winds and wind reversal is notable. Although the subset does not capture the intra-seasonal variability shown in the full set due to the more strongly constrained maximum wind speed, the correlation between the two daily time series reaches a fairly high correlation of 0.5–0.6 reflecting a significant degree of self-consistency in the CIPS cloud tracking winds on the day-to-day variability. We also rely on this self-consistency to remove the days at the start and end of the season during which the day-to-day variability patterns of the full set and subset notably contradict each other. As a result the length of daily time series slightly varies with year.

The NOGAPS zonal winds at the (CIPS wind) coincidences show drastically different intra-seasonal variability. Due to the generally much stronger westward winds throughout the season, in NOGAPS the timings of the seasonal wind reversal are extended back into May or April depending on the LT ranges. It is especially noteworthy that the NOGAPS zonal winds are strengthened in August relative to June and July, which is not echoed in the CIPS result or in the wind climatology [Portnyagin 2004b; Lukianova et al., 2018]. As Eckermann et al. [2009] has stated, tuning the gravity wave drag can significantly affect the mean and tidal structures which may be able to interpret this bias but there does not seem to be an apparent anomaly in temperature or geopotential height gradient associated with the larger August winds. It is also worth mentioning that the NOGAPS zonal winds sampled at the 2009 and 2007 CIPS coincidences hold a correlation of 0.7 which suggests that the zonal wind variability is only mildly affected by the sampling details reflecting a robust intra-seasonal variation pattern.

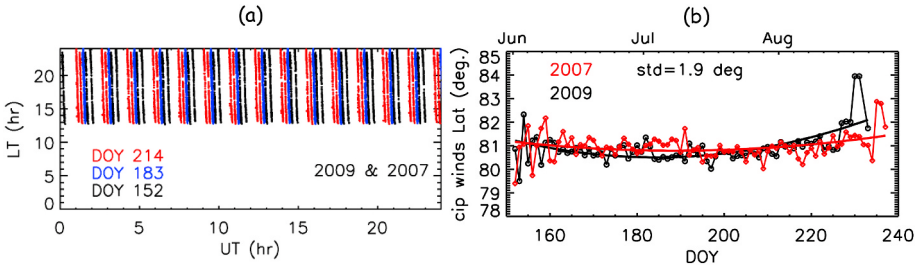

Fig. 11. (a) The CIPS local time coverage demonstrated over three days in the two selected years. (b) The daily mean latitude time series of the CIPS wind detections. The averaged standard deviation (STD) throughout the season is given in the legend. The smooth curves are 2nd order polynomial fits.

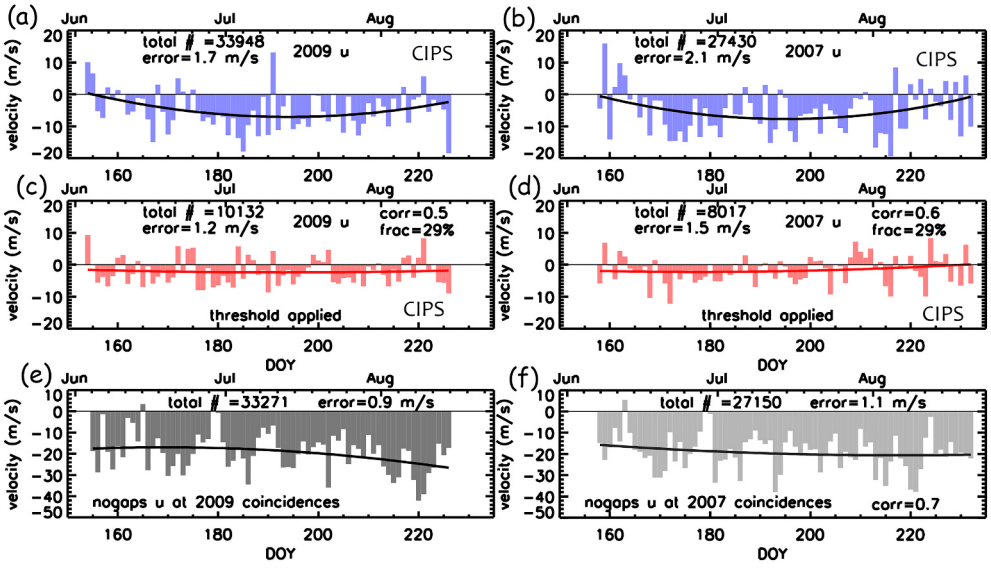

Fig. 12. The daily mean U series in the CIPS winds (a–d) and the counterpart in NOGAPS winds sampled at the CIPS coincidences (e–f). The number of detections throughout the season and the seasonal mean of daily standard error of mean (SEM) are indicated in the legend. The (a) and (c) or (b) and (d) are pairs of with and without wind thresholds in CIPS. The more "reliable" CIPS wind subsets are about 29% of the total wind detections, as marked. The “corr” numbers in the legends in the middle panels are the correlation coefficients between (a) and (c), (b) and (d) respectively. The “corr” number in the legend in (f) is the correlation coefficient between (e) and (f). All fitting curves are 2nd order polynomials.

The results for the meridional winds are shown in Fig. 13. The 2nd order polynomial fitting curves suggest 2–5 m/s of outflow from the pole in the core of the season which is qualitatively consistent with the climatology. It is especially striking to note that the variability patterns in the CIPS meridional winds differ so drastically between 2007 and 2009; in 2009 there are smaller (meridional) winds in the middle of the season than toward the start and end; in 2007 it is the opposite. The CIPS wind subsets with smaller speeds show qualitatively the same results as in their full sets; in 2009 however, a larger discrepancy exists in the beginning of June which worsens the correlation between the two curves to about 0.4, otherwise they agree well throughout July and August. This correlation reaches 0.7 in 2007, reflecting the excellent consistency between the full wind set and the subset.

The NOGAPS meridional winds sampled at the 2009 and 2007 CIPS wind coincidences yield the same inter-annual difference, which is not expected. We so far have not identified any mechanism that would support this consistency since the NAVDAS system assimilated the satellite data in 2009 exclusively. In this particular case however, the difference in NOGAPS is caused by the coincidences residing on the ascending and descending parts of the orbits respectively in the two years; we are aware that CIPS orbits in 2009 and 2007 approximately repeat, but the ascending and descending nodes are located in different lon sections. Unlike in the zonal winds, the daily time series of the NOGAPS meridional winds sampled at the 2009 and 2007 coincidences show a weak correlation of 0.2, reflecting the strong impact of the sampling details in the meridional winds. The NOGAPS analysis so far indicates that the intra-seasonal variability of the meridional winds is susceptible to different sampling path and therefore does not conform to an established pattern. In the zonal winds, on the other hand, although the sampling difference from day-to-day also causes the daily value to change it is not sufficient to alter the longer time scale intra-seasonal variability.

Partial LT coverage is considered a major cause of the overall weaker CIPS zonal winds. To elaborate this, we presented the intra-seasonal variations of the daily mean NOGAPS zonal winds averaged over the CIPS LT range and over the full 0–24 h LT range respectively in Fig. 14.

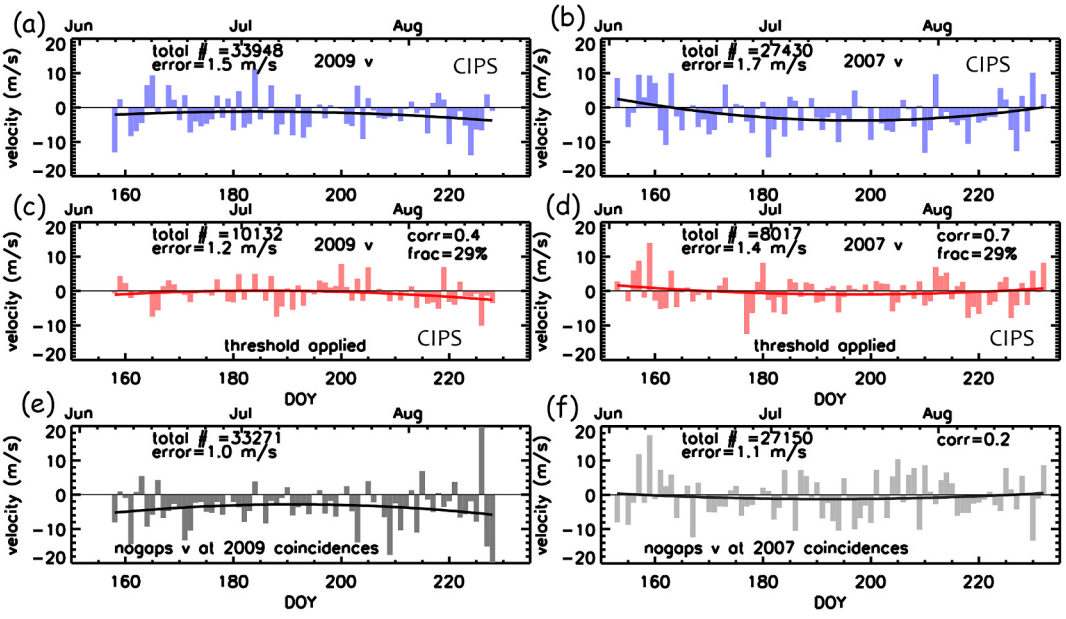

Fig. 13. Same as Fig. 12 except for the meridional wind (V).

All grid points on the surface of 0.00436 hPa in the latitudinal range 70°–86°N are used in this analysis. It is striking to note that the winds sampled at the 13–23 h LT range are systematically weaker by about 8–10 m/s throughout the season, with the day-to-day variability kept almost intact. This will partially interpret the overall smaller zonal winds in the CIPS wind set and also indicates that with only half of the LT coverage the zonal wind intra-seasonal variation pattern is not affected. The polynomial fitting curves suggest very mild acceleration/deceleration in early June and late August, confirming that NOGAPS zonal winds are persistently strong in these months. The uncertainty in the NOGAPS daily time series of the zonal winds reaches ~1.5 m/s reflecting the same degree of spatial variability as in the CIPS winds. In addition, the 2–10day variability in the time series with amplitude of roughly ~10 m/s reflects the wavenumber-zero low frequency fluctuation modes since both spatial variability and tides are eliminated by the averaging process.

The NOGAPS daily mean meridional winds averaged over the two LT ranges (shown in Fig. 14b) exhibit highly suppressed daily fluctuation amplitudes with the wind speed remaining almost constant at 2–3 m/s throughout the season. This reflects the strong cancellation of different variability modes in the meridional winds. Given the suppressed amplitude, the daily time series for the two LT ranges are able to achieve a correlation coefficient of 0.5 reflecting a significant degree of self-consistency in the wavenumber-zero low frequency fluctuation modes. Although the overall magnitude differences between the two curves are small, the intra-seasonal variation patterns of the two LT ranges are qualitatively different; in the middle of the season the wind is about 1.0 m/s smaller in the CIPS LT range, whereas the values converge at the start and end of the season.

We next briefly compare the CIPS winds with the Horizontal Wind Model 2014 (HWM14) [Drob et al., 2015] climatology. The HWM models are primarily utilized in the studies of the Earth upper atmosphere and are not much referenced in the mesospheric studies. Nevertheless the quiet time component of HWM provides the climatological horizontal winds from the ground to the exobase (~500 km altitude) as a function of day of year, solar local time, colatitude, and longitude. The atmosphere's dominant recurring cyclical climatological variations, i.e., predominantly seasonal and diurnal, are represented by height-modulated vector spherical harmonic basis functions. The HWM experienced a sequence of earlier versions such as HWM87, 90, 93, and 07. The HWM07 [Drob et al., 2008] and HWM 14 share the same observational database for winds below the mesopause, among which UARS HRDI [Hays et al., 1993], sounding rockets [Schmidlin et al., 1985], and medium-frequency radar [Murayama et al., 2000] were the listed data sets used to construct the winds in the northern PMC region.

The HWM14 zonal winds averaged daily in the latitude range 70°–86°N exhibit a prolonged acceleration throughout June to mid-July and a deceleration in the remaining of the season. The intra-seasonal variability is more distinct than in the NOGAPS zonal wind polynomial fit. But it is especially enlightening to observe that the daily time series using all local times and using only the 13–23 h LT range are shifted by ~6–8 m/s consistently throughout the season while sharing extremely similar intra-seasonal variation pattern. This LT dependence strongly agrees with the NOGAPS result, verifying that LT range is a key factor to determine the magnitude of the zonal winds, and both point to the dominant impact of the diurnal migrating tides. The overall zonal wind magnitude in the HWM14 is about ~5–7 m/s larger than the polynomial fits of the CIPS zonal winds. Although the HWM14 zonal winds show distinct asymmetry between June and August, this condition changes when the altitude surface is chosen to be at 80 km or 85 km, indicating that it is not a robust feature.

The HWM14 meridional winds in Fig. 14b show qualitatively different results between the two LT ranges, characterized by the reversed signs between the two time series prior to late July and drastically different intra-seasonal variation patterns. Although having opposite directions, both HWM14 and NOGAPS meridional winds in the LT range 13–23 h maintain fairly constant speeds throughout the season. The condition of HWM14 consistently picking up the northward winds in the CIPS LT range is caused by the dominant migrating tides in the model (not shown here). On the contrary, in the NOGAPS meridional winds the LT dependence strongly varies between the different lons, reflecting the presence of many other scales including the non-migrating tides.

6. Planetary scale wave analysis to the NOGAPS winds

Polar summer mesosphere is under control of a wide spectrum of the planetary scale slow waves and tides, and these variability modes are thought to be excited by the winter polar night jet instability and the further wave ducting activity [Garcia et al., 2005]. Merkel et al. [2009] shows that CIPS PMC albedo analysis indicates multiple peaks with the westward traveling 5day wavenumber-1 and eastward traveling 2day wavenumber-1 as the dominant components. Other components such as 2day and 5day wavenumber-2 are also present. However, caution should be used when applying regression analysis to the CIPS winds because the data coverage is too poor to resolve tides which are considered the dominant variability modes in the mesospheric winds [e.g., Stober et al., 2012]. The asynoptic coverage of satellite orbits will result in aliasing of the (non-migrating) tidal variability onto the 2–5day variability in the intra-seasonal time series [e.g., Salby, 1982; Talaat and Lieberman, 1999].

In this section we aim to briefly evaluate the results of the NOGAPS zonal winds regressed against the tidal components and the 2–5day planetary wave components, in order to demonstrate the possible aliasing effect due to the asynoptic sampling of the CIPS winds. For a single analysis, we generate the lon series of winds averaged north of 75°N for each 1.5° of lon bin for each UT hour and the same process repeats for a 10-day period. Fig. 16a shows the lon vs. time map of the NOGAPS zonal winds on the DOYs 185–195, along with the over-plotted CIPS wind coverage denoted by white dots. In Figs. 16b–c the superimposed westward and eastward propagating tidal components are shown respectively. In this analysis the diurnal, semidiurnal, and tri-diurnal tides are included, and the zonal wavenumber ranges from 0 to 6. Figs. 16b and 16c indicate that westward propagating tides are notably stronger. In addition, it is especially noteworthy that in Fig. 16b the CIPS winds fell almost exactly at the ridges of the westward propagating tidal variability modes, which further confirms why CIPS westward winds are systematically weaker, as shown in Figs. 14a and 15a. On the other

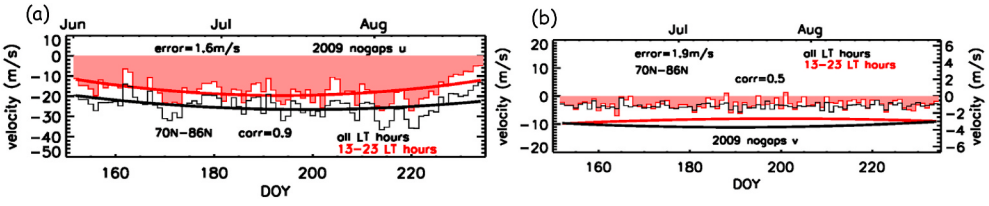

Fig. 14. (a)–(b) The NOGAPS wind daily mean series (U and V) using all data in 70°–86°N (black curves) and using the data exclusively in the CIPS local time range (13–23 h, red fills). The thick smooth curves are 2nd order polynomial fits. Note that in (b) the smooth curves used the right vertical axis for scale for better presentation.

hand, from observing Fig. 16c we are able to confirm that CIPS sampling will pick up variability from the eastward propagating tides and be aliased onto longer time scale variability.

The statistics of the regression analyses for the sliding 10-day windows throughout the PMC season indicate that tidal variability is dominant over the 2–5day planetary wave variability. Different combinations of the harmonic components are used to reconstruct the lon vs. time map of the NOGAPS zonal winds. The corresponding histograms are then yielded via sampling the correlation coefficients between the reconstructed map and the original NOGAPS zonal wind map, shown in Fig. 17a. In Fig. 17b it further indicates that the correlation coefficient is an excellent proxy to the mean-amplitude-ratio between the reconstructed (lon vs. time) map and the original NOGAPS map, with the mean amplitude being defined as the square-root of the variance. When tides and the 2–5day planetary waves are combined, the histogram peaks at a correlation coefficient of 0.6 which also indicates that about 60% of the amplitude can be accounted for using these components. The thick purple and black histograms maximize closely to each other suggesting that the main contribution is from tides. In comparison, the 2–5day planetary wave components collectively contribute to about 27% of the variability on average which is substantially smaller than those from tides. In both tides and the 2–5day planetary waves, the westward propagating components are dominant, characterized by the notable separation between the histograms in turquoise and blue, or in orange and yellow-green, respectively. After closer examination, we found that the westward and the eastward propagating 2–5day planetary waves contribute to about 20% and 10% of the variability respectively; the two percentages are overall much smaller and meanwhile differ less than those for the tides. Yet CIPS sampling will also cause aliasing between the westward and eastward propagating 2–5day variability modes.

7. Remaining issues

The CIPS wind product is fairly robust, reflected in the daily time series of zonal winds using the 1.5 ° × 1.5 ° and 4.5 ° × 4.5 ° sampling grids respectively in Fig. 18. Although the overall wind population is halved in the coarser sampling grid their intra-seasonal variation patterns are tremendously consistent with noteworthy magnitude differences, suggesting that the preliminary CIPS wind set has achieved sufficient redundancy after merging the products from using the three frame sizes. We may in the future increase the redundancy through further splitting the 1/3 frame-size step into finer steps to examine whether it will improve the accuracy of the wind product.

The stereoscopic parallax is considered a minor error source to the CIPS winds because cloud height uncertainty is relatively small (±3 km) [Russell et al., 2010] and in the meantime the time interval between the two progressive patterns is relatively long (~96 min). The height uncertainty will affect the wind determination through affecting the lon and lat registration. The retrieved lons and lats are included in the CIPS level-2 data, and a separate investigation is required to determine the extent to which the parallax will affect the lon and lat registration given the cloud deck height varying by ±3 km.

The primary uncertainty in the CIPS wind tracking lies in the fact that 96 min are a fairly long time period so that the wave dynamics will cause variations in the PMC ice mass and further affect the pattern recognition. In fact this is the main reason why the CIPS cloud pattern matching has a relative low success rate (see Fig. 1b). We argued above that between two adjacent CIPS orbits the pattern could be roughly conserved even though the overall brightness level is changed due to large scale waves. Future validation will be required to further assess whether the long term operation of the CIPS PMC tracking is a worthwhile endeavor.

Future cloud wind tracking should also include the pre-screening of the cloud features [Mueller et al., 2013]. For example, the framed cloud features that possess low contrast and high noise of albedo should be removed. The cloud feature contrast can be characterized by the albedo amplitude for the largest scale variability within the matching frame [Rong et al., 2018].

The evolution of the small scale gravity wave structures enclosed in the matching frames is another interest of ours in the context of the CIPS cloud tracking. We will conduct the investigation beyond the case studies via obtaining the statistical results throughout the entire season and different years. Such small scale wave structures (i.e., ~20–60 km) often vary by some degree but remain as semi-organized between two consecutive orbits. The CIP cloud tracking is an appropriate platform to examine whether they are the same wave structure transported by wind advection and how they have evolved between the two time stamps [e.g., Fogle and Haurwitz, 1966].

8. Conclusions

We have thoroughly described the refined CIPS PMC wind tracking algorithm and assessed its first product relative to the NOGAPS winds and the HWM14 wind climatology. The sanity of the wind set is validated but more years of CIPS wind data are required to further assess whether CIPS cloud tracking is a reliable approach to create the long time series of the mesopause winds in the polar summer region.

The CIPS zonal winds and meridional winds are westward and southward statistically, which conforms to the established wind climatology. The CIPS zonal wind speed is contained within 20 m/s throughout the season and is about 5–10 m/s smaller than the NOGAPS or HWM14 winds in the corresponding LT range. The apparent cause of the smaller CIPS winds is likely the limitation on the allowed distance for frame movement even though there are occasions that cloud tracking result clearly indicates smaller winds than in the NOGAPS at the coincidences. The CIPS meridional wind speed is within 10 m/s throughout the season which is very close to the NOGAPS result.

For effective cloud tracking, the frame size for the cloud pattern matching shall be far greater than the pixel size and the movement of a full frame size shall be correspondent to the roughly maximum wind speed. We adopted three frame sizes which are 500 km as the default size used before, and 25% smaller and larger sizes respectively. Each given size refers to the length in the lon direction at the lowest lat of the frame. Choosing multiple frame sizes is to generate redundant wind detections to eventually achieve more robust wind set with better consistency and

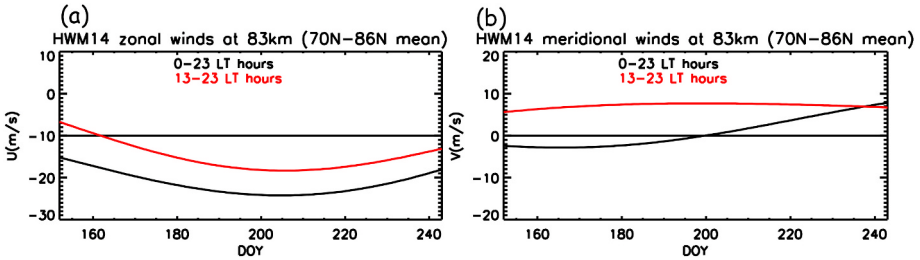

Fig. 15. Same as Fig. 14 except using the Horizontal Wind Model 2014 (HWM14) output.

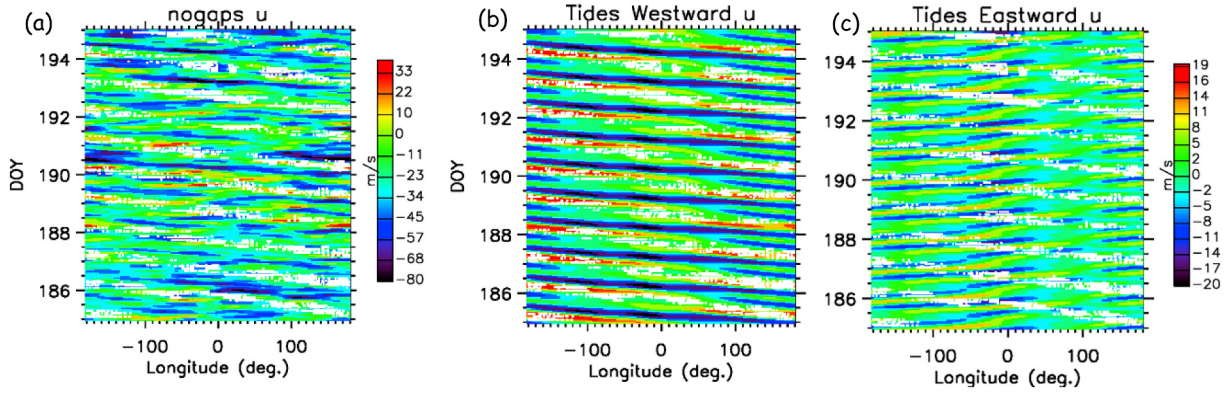

Fig. 16. (a) Lon vs. time map of NOGAPS zonal winds over a 10-day period spanning DOYs 185-185 2009. For each 1.5° of lon bin and each UT hour, latitudinal average in the range 70°–86°N is used. (b) Superimposed westward propagating tides including diurnal, semidiurnal, and tri-diurnal with wavenumbers ranging from 0 to 6. (c) Eastward propagating tidal components. The white dots are lons and times at the CIPS wind detections for this 10-day period.

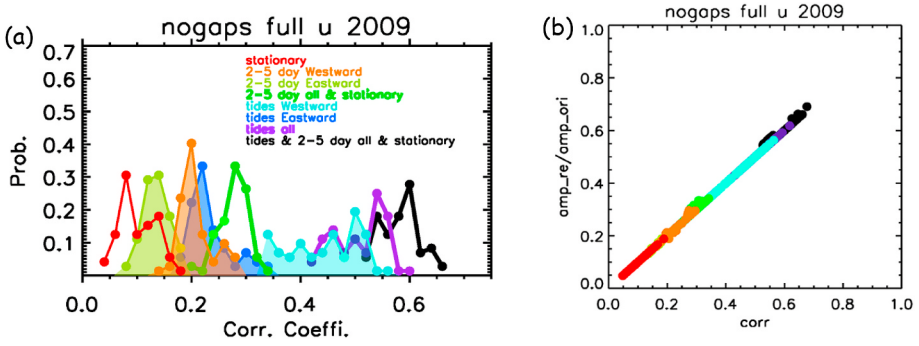

Fig. 17. (a) Histograms of the correlation coefficients between the different combinations of harmonic components and the original lon vs. time map of the NOGAPS zonal winds, indicated in the legends. Each correlation coefficient is for one 10-day period and the statistics is for the sliding 10-day windows throughout the PMC season with 1-day increments. (b) Scatter plot between the correlation coefficients and the corresponding mean-amplitude-ratios. Each correlation coefficient or mean-amplitude-ratio is calculated between the superimposed harmonic components and the original lon vs. time map. The mean amplitude refers to the square-root of the variance.

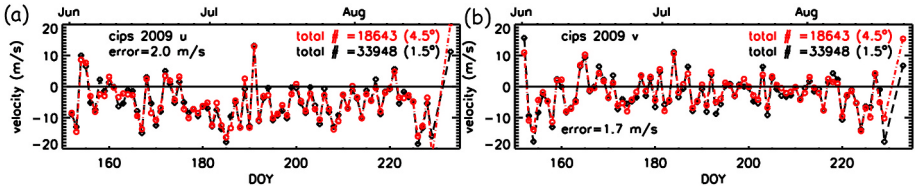

Fig. 18. (a–b) Daily time series of the CIPS cloud tracking winds (U and V) in 2009, screened and edited within grids 1.5 ° × 1.5 ° (black) and 4.5 ° × 4.5 ° (red), respectively. The error is the averaged SEM throughout the season and the two sampling grid sizes. Other numbers in the legends have the same meaning as in Fig. 12.

spatial coverage. In the CIPS PMC tracking algorithm the best match of a given cloud pattern is searched within one default frame size in both lon and lat directions. Eventually achieving maximum Pearson correlation that exceeds 0.7 is used as the criterion of a successful match.

The rationale of the frame size choice is explored via examining the CIPS PMC cloud feature memory, characterized by the correlation coefficient of the cloud feature within the same frame location between two adjacent orbits in the level-2 data. Better memory will lead to higher success rate of the pattern matching in the actual cloud wind tracking. The CIPS PMCs "remember" increasingly better of their history from 96 min ago when the frame size encloses larger area of cloud features, but we should keep in mind that choosing larger frame will practically reduce the number of independent cloud patterns which will eventually reduce the number of wind detections.

Preliminary wind sets from the three frame sizes are first merged, and then screening/editing is applied within each regularly spaced grid-cell to eventually obtain a wind that is representative. In our first wind product the sampling grid-sizes used are 1.5°lon × 1.5°lat and 4.5°lon × 4.5°lat respectively, to test the self-consistency and the data quality. Within each grid-cell, winds are grouped into different clusters by similar directions (±20°). If a wind does not pair up with any other wind in the grid-cell it is removed as an anomaly. Different clusters are averaged eventually to obtain the mean wind in the grid-cell; if there is not any cluster then we select the wind with the minimum speed.

There is a definitive but low degree of deterministic consistency between the CIPS and NOGAPS winds at the coincidences. The agreements are widespread at all lons on CIPS orbits but the number of agreements (per orbit) is highly unbalanced between different orbits. Averaging over all orbits, the two wind sets can achieve about ~30% agreements if both the zonal and meridional winds are required to be in the consistent directions. The wind agreement and the ice distribution consistency have shown a quantitative causal link on the orbit-by-orbit basis, indicating that temperature is probably impacting both. The discrepancy could be due to three factors. First, the NAVDAS component is incorporated 6-hourly rather than 1-hourly and therefore the NOGAPS temperature is deviated from the true temperature. This would affect the accuracy of both 0-D modeled ice and the NOGAPS winds; second, the CIPS winds contain ageostrophic components and are cascaded into smaller scales compared to the NOGAPS winds. Third, the CIPS cloud tracking approach may have led to false wind detections.

The CIPS zonal (westward) winds are decreased and reversed in early June and late August whereas in the core of the season they are stronger. This overall variation pattern is shared by both NOGAPS and HWM14 zonal winds, but the magnitudes and the detailed intra-seasonal variability differ between years or wind sets. For example, the NOGAPS zonal winds are persistently strong throughout the June, July, and August exhibiting a very mild intra-seasonal variability. It is especially noteworthy that the NOGAPS zonal winds averaged over the CIPS LT range (~13–23 h) are ~8–10 m/s smaller than using all data in the 0–24 h LT times. The same LT dependence is echoed in the HWM14 zonal winds, which may partially interpret the systematically smaller CIPS zonal winds.

The meridional (equatorward) winds do not follow any established intra-seasonal variation pattern but rather the variability is susceptible to the sampling lons/lats on a daily basis. The CIPS winds in 2009 and 2007 exhibit drastically different intra-seasonal variation patterns. The NOGAPS winds sampled at the coincidences (with CIPS) in these two years also show the same inter-annual difference that is apparently caused by sampling on the ascending and descending nodes respectively. The HWM14 meridional wind climatology averaged in the CIPS LT range are persistently poleward, mainly due to the presence of distinctly dominant migrating tides. On the contrary, the NOGAPS meridional winds exhibit more complex tidal variability so that spatial averaging strongly suppresses the daily fluctuation. These results overall suggest that the meridional wind variability is dependent on the sampling path therefore more unpredictable, which is very different from the zonal winds.

Regression analyses applied to the lon vs. time maps of NOGAPS zonal winds spanning the 10-day periods indicate that both tides and 2–5day variability modes contribute substantially in the zonal wind variability but the tidal variability is dominant. Especially, when non-migrating tides are present, as is the case in the NOGAPS winds, aliasing can be significant when planetary wave analysis is applied to asynoptic data such as the CIPS cloud tracking winds.

Declaration of competing interest

The authors declare that they have no known competing financial interests or personal relationships that could have appeared to influence the work reported in this paper.

Acknowledgement

This work was supported by the NSF CEDAR: United States award ID1651394 and NASA Small Explorer Program: United States through contract NAS5-03132. We thank the NRL for providing the NOGAPS-ALPHA data. We are also extremely grateful to Dr. Douglas Drob for providing the Horizontal Wind Model (HWM14). We acknowledge all members of AIM science team, especially the CIPS science team and retrieval team, for their support on this project throughout the years. CIPS data can be accessed through website http://lasp.colorado.edu/aim/download-data-pmc.php. We are also grateful to Dr. Dong L. Wu from NASA and Dr. Jie Gong from USRA for providing the initiatives in the early stage of this research project.

References

Bailey, S.M., Randall, C.E., Lumpy, J.D., Hervig, M.E., Thomas, G.E., Russell, J.M., 2009. Phase functions of polar mesospheric cloud ice as observed by the CIPS instrument on the AIM satellite. J. Atmos. Sol. Terr. Phys. 71, 373–380. https://doi.org/10.1016/j.jastp.2008.09.039.

Baumgarten, G., Lübken, F.-J., Fricke, K.H., 2002. First observation of one noctilucent cloud by a twin lidar in two different directions. Ann. Geophys. 20 (11), 1863–1868.

Berger, U., von Zahn, U., 2007. Three-dimensional modeling of the trajectories of visible noctilucent cloud particles: an indication of particle nucleation well below the mesopause. J. Geophys. Res. 112, D16204. https://doi.org/10.1029/2006JD008106.

Dalin, P., et al., 2013. Optical studies of rocket exhaust trails and artificial noctilucent clouds produced by Soyuz rocket launches. J. Geophys. Res. Atmos. 118, 7850–7863. https://doi.org/10.1002/jgrd.50549.

Dowdy, A.J., Vincent, R.A., Tsutsumi, M., Igarashi, K., Murayama, Y., Singer, W., Murphy, D.J., 2007. Polar mesosphere and lower thermosphere dynamics: 1. Mean wind and gravity wave climatologies. J. Geophys. Res. 112, D17104. https://doi.org/10.1029/2006JD008126.

Drob, D.P., et al., 2008. An empirical model of the Earth's horizontal wind fields: HWM07. J. Geophys. Res. 113, A12304. https://doi.org/10.1029/2008JA013668.

Drob, D.P., et al., 2015. An update to the Horizontal Wind Model (HWM): the quiet time thermosphere. Earth and Space Science 2, 301–319. https://doi.org/10.1002/2014EA000089.

Eckermann, S.D., Hoppel, K.W., Coy, L., McCormack, J.P., Siskind, D.E., Nielsen, K., Kochenash, A., Stevens, M.H., Englert, C.R., Hervig, M., 2009. High-altitude data assimilation system experiments for the northern summer mesosphere season of 2007. J. Atmos. Sol. Terr. Phys. 71, 531–551.

Eckermann, S.D., McCormack, J.P., Coy, L., Allen, D., Hogan, T., Kim, Y-J., 2004. NOGAPS-ALPHA: A PROTOTYPE HIGH-ALTITUDE GLOBAL NWP MODEL. Symposium on the 50th. Anniversary of Operational Numerical Weather Prediction, P2.6. American Meteorological Society.

Foerster, W., Jesse, O., 1892. Invitation to observe the luminous night clouds. Nature 46, 589–590. https://doi.org/10.1038/046589a0.

Fogle, B., Haurwitz, B., 1966. Noctilucent clouds. Space Sci. Rev. 6 (3), 279–340.

Fritts, D.C., Laughman, B., Lund, T.S., Snively, J.B., 2015. Self-acceleration and instability of gravity wave packets:1. Effects of temporal localization. J. Geophys. Res. Atmos. 120, 8783–8803. https://doi.org/10.1002/2015JD023363.

Fujita, T.T., Bradbury, D.L., Murino, C., Hull, L., 1968. A Study of Mesoscale Cloud Motions Computed from ATS-I and Terrestrial Photographs. SMRP Paper, vol. 71. The University of Chicago.

Fujita, T.T., Pearl, E.W., Shenk, W.E., 1973. SATELLITE-TRACKED CUMULUS VELOCITIES, SMRP Paper 114. The University of Chicago.

Garcia, R.R., 1989. Dynamics radiation and photochemistry in the mesosphere: implication for the formation of the noctilucent clouds. J. Geophys. Res. 94 (D12 14), 605–614, 615.

Garcia, R.R., Solomon, S., 1985. The effect of breaking gravity waves on the dynamics and chemical composition of the mesosphere and lower thermosphere. J. Geophys. Res. 90 (D2), 3850–3868. https://doi.org/10.1029/JD090iD02p03850.

Garcia, R.R., Lieberman, R., Russell III, J.M., Mlynczak, M.G., 2005. Large-scale waves in the mesosphere and lower thermosphere observed by SABER. J. Atmos. Sci. 62, 4384–4399.

Hays, P.B., Abrue, V.J., Dobbs, M.E., Gell, D.A., Grassl, H.J., Skinner, W.R., 1993. The high-resolution Doppler imager on the upper atmosphere research satellite. J. Geophys. Res. 98 (10) https://doi.org/10.1029/93JD00409, 713 – 10,723.

Hervig, M.E., Stevens, M.H., Gordley, L.L., Deaver, L.E., Russell III, J.M., Bailey, S.M., 2009. Relationships between PMCs, temperature and water vapor from SOFIE observations. J. Geophys. Res. 114, D20203. https://doi.org/10.1029/2009JD012302.

Hoffmann, P., Rapp, M., Singer, W., Keuer, D., 2011. Trends of mesospheric gravity waves at northern middle latitudes during summer. J. Geophys. Res. 116, D00P08. https://doi.org/10.1029/2011JD015717.

Horváth, Á., Davies, R., 2001. Feasibility and error analysis of cloud motion wind extraction from near-simultaneous multiangle MISR measurements. J. Atmos. Ocean. Technol. 18, 591–608. https://doi.org/10.1175/1520-0426(2001)018,0591.FAEAOC.2.0.CO;2.

Jensen, E., Thomas, G.E., 1988. A growth-sedimentation model of polar mesospheric clouds: comparison with SME measurements. J. Geophys. Res. 93, 2461–2473. https://doi.org/10.1029/JD093iD03p02461.

Latteck, R., Singer, W., Rapp, M., Vandepeer, B., Renkwitz, T., Zecha, M., Stober, G., 2012. MAARSY: the new MST radar on Andøya-System description and first results. Radio Sci. 47, RS1006. https://doi.org/10.1029/2011RS004775.

Lübken, F.-J., Müllemann, A., 2004. Temperatures and horizontal winds in the Antarctic summer mesosphere. J. Geophys. Res. 109, D24112. https://doi.org/10.1029/2004JD005133.

Lukianova, R., Kozlovsky, A., Lester, M., 2018. Climatology and inter-annual variability of the polar mesospheric winds inferred from meteor radar observations over Sodankylä (67N, 26E) during solar cycle 24. JASTP 171, 241–249, 2018.

Lumpe, J.D., et al., 2013. Retrieval of polar mesospheric cloud properties from CIPS: algorithm description, error analysis and cloud detection sensitivity. J. Atmos. Sol. Terr. Phys. 104, 167–196. https://doi.org/10.1016/j.jastp.2013.06.007.

McClintock, W.E., Rusch, D.W., Thomas, G.E., Merkel, A.W., Lankton, M.R., Drake, V.A., Bailey, S.M., Russell III, J.M., 2009. The cloud imaging and particle size experiment on the Aeronomy of Ice in the Mesosphere mission: instrument concept, design, calibration, and on-orbit performance. J. Atmos. Sol. Terr. Phys. 71, 340–355. https://doi.org/10.1016/j.jastp.2008.10.011.

McCormack, J.P., Coy, L., Hoppel, K.W., 2009. Evolution of the quasi 2-day wave during January 2006. J. Geophys. Res. 114, D20115. https://doi.org/10.1029/2009JD012239.

McCormack, J.P., Coy, L., Singer, W., 2014. Intraseasonal and interannual variability of the quasi 2day wave in the Northern Hemisphere summer mesosphere. J. Geophys. Res. Atmos. 119, 2928–2946. https://doi.org/10.1002/2013JD020199.

Menzel, W.P., 2001. Cloud tracking with satellite imagery: from the pioneering work of Ted Fujita to the present. Bull. Am. Meteorol. Soc. 82 (2), 33–47. https://doi.org/10.1175/1520-0477(2001)082<0033:CTWSIF>2.3.CO.

Merkel, W.A., Rusch, D.W., Palo, S.E., Russell III, J.M., Bailey, S.M., 2009. Mesospheric planetary wave activity inferred from AIM-CIPS and TIMED-SABER for the northern

summer 2007 PMC season. J. Atmos. Sol. Terr. Phys. https://doi.org/10.1016/j.jasp.2006.05.01.

Mertens, C.J., et al., 2004. SABER observations of mesospheric temperatures and comparisons with falling sphere measurements taken during the 2002 summer MaCWAVE campaign. Geophys. Res. Lett. 31, L03105.

Mueller, K., Moroney, C., Jovanovic, V., Garay, M.J., Muller, J.-P., Girolamo, L.D., Davies, R., 2013. MISR Level 2 Cloud Product Algorithm Theoretical Basis. JPL D-73327.

Mueller, K.J., Wu, D.L., Horváth, Á., Jovanovic, V.M., Muller, J.-P., DI Girolamo, L., Garay, M.J., Diner, D.J., Moroney, C.M., Wanzong, S., 2017. Assessment of MISR cloud motion vectors (CMVs) relative to GOES and MODIS atmospheric motion vectors (AMVs). J. APP. METEO. AND CLIM. https://doi.org/10.1175/JAMC-D-16-0112.1.

Murayama, Y., Igarashi, K., Rice, D., Watkins, B., Collins, R., Mizutani, K., Saito, Y., Kainuma, S., 2000. Medium frequency radars in Japan and Alaska, for upper atmosphere observations. IEICE Trans. Fund. Electron. Commun. Comput. Sci. E83-B, 1996–2003.

Portnyagin, Y., et al., 2004a. Monthly mean climatology of the prevailing winds and tides in the Arctic mesosphere/lower thermosphere. Ann. Geophys. 22, 3395–3410. https://doi.org/10.5194/angeo-22-3395-2004.

Portnyagin, Y., et al., 2004b. Mesosphere/lower thermosphere prevailing wind model. Adv. Space Res. 34, 1755–1762.

Rapp, M., Lübken, F.-J., Müllemann, A., Thomas, G.E., Jensen, E.J., 2002. Small scale temperature variations in the vicinity of NLC: experimental and model results. J. Geophys. Res. 107 (D19), 4392. https://doi.org/10.1029/2001JD001241.

Renkwitz, T., Tsutsumi, M., Laskar, F.I., Chau, J.L., Latteck, R., 2018. On the role of anisotropic MF/HF scattering in mesospheric wind estimation. Earth Planets Space 70, 158. https://doi.org/10.1186/s40623-018-0927-0.

Rong, P.P., Yue, J., Russell III, J.M., Lumpe, J.D., Gong, J., Wu, D.L., Randall, C.E., 2015. Horizontal winds derived from the polar mesospheric cloud images as observed by the CIPS instrument on the AIM satellite. J. Geophys. Res. Atmos. 120, 5564–5584. https://doi.org/10.1002/2014JD022813.

Rong, P.P., Yue, J., Russell III, J.M., Siskind, D.E., Randall, C.E., 2018. Universal power law of the gravity wave manifestation in the AIM CIPS polar mesospheric cloud images. Atmos. Chem. Phys. 18, 883–899. https://doi.org/10.5194/acp-18-883-2018.

Russell, J.M.I.I.I., et al., 2009. Aeronomy of Ice in the Mesosphere (AIM) mission: overview and early science results. J. Atmos. Sol. Terr. Phys. 71 (3–4), 289–299. https://doi.org/10.1016/j.jastp.2008.08.011.

Russell, J.M.I.I.I., Rong, P., Bailey, S.M., Hervig, M.E., Petelina, S.V., 2010. Relationship between the summer mesopause and polar mesospheric cloud heights. J. Geophys. Res. 115, D16209. https://doi.org/10.1029/2010JD013852.

Salby, M.L., 1982. Sampling theory for asynoptic satellite observations. Part II: fast Fourier synoptic mapping. J. Atmos. Sci. 39, 2601–2614.

Schwartz, M.J., et al., 2008. Validation of the aura microwave limb sounder temperature and geopotential height measurements. J. Geophys. Res. 113, D15S11.

Siskind, D.E., Drob, D.P., Emmert, J.T., Stevens, M.H., Sheese, P.E., Llewellyn, E.J., Hervig, M.E., Niciejewski, R., Kochenash, A.J., 2012. Linkages between the cold summer mesopause and thermospheric zonal mean circulation. Geophys. Res. Lett. 39, L01804. https://doi.org/10.1029/2011GL050196.

Stevens, M.H., et al., 2010. Tidally induced variations of polar mesospheric cloud altitudes and ice water content using a data assimilation system. J. Geophys. Res. 115, D18209. https://doi.org/10.1029/2009JD013225.

Stevens, M.H., Lieberman, R.S., Siskind, D.E., McCormack, J.P., Hervig, M.E., Englert, C. R., 2017. Periodicities of polar mesospheric clouds inferred from a meteorological analysis and forecast system. J. Geophys. Res. Atmos. 122 https://doi.org/10.1002/2016JD025349.

Stober, G., Latteck, R., Rapp, M., Singer, W., Zecha, M., 2012. Maarsy – the new MST radar on Andøya: first results of spaced antenna and Doppler measurements of atmospheric winds in the troposphere and mesosphere using a partial array. Adv. Radio. Sci. 10, 291–298. www.adv-radio-sci.net/10/291/2012/doi:10.5194/ars-10-291-2012.

Talaat, E.R., Lieberman, R.S., 1999. Nonmigrating diurnal tides in mesospheric and lower-thermospheric winds and temperatures. J. Atmos. Sci. 56 (24).

Wu, D.L., Halpern, D., Mueller, K.J., Rodriguez, E., Kavaya, M.J., Singh, U.N., Tucker, S., Emmitt, G.D., Ruf, C.S., Horváth, Á., 2015. NASA Global Wind Measurements and Technology Development, CGMS-43 NASA-WP-05, V1, 18 May 2015.

Schmidlin et al. (1985), Rocket techniques used to measure the neutral atmosphere, International Council of Scientific Unions Middle Atmosphere Program: Handbook for MAP, vol. **19**, edited by **R. A. Goldberg**, pp. **1 – 28**, **Inst. of Appl. Geophys., Moscow**.